SOLID-STATE ARRAYS AND BEAMFORMERS FOR SIDE-LOOKING INTRAVASCULAR ULTRASONIC IMAGING

ALPER ŞİŞMAN

B.S., Electrical Engineering, Istanbul Technical University, 1998

M.S., Electronics Engineering, Işık University, 2002

Submitted to the Graduate School of Science and Engineering
in partial fulfillment of the requirements for the degree of
Doctor of Philosophy
in
Electronics Engineering

IŞIK UNIVERSITY
2010

IŞIK UNIVERSITY
GRADUATE SCHOOL OF SCIENCE AND ENGINEERING

SOLID-STATE ARRAYS AND BEAMFORMERS FOR SIDE-LOOKING INTRAVASCULAR ULTRASONIC IMAGING

ALPER ŞİŞMAN

.

APPROVED BY:

Prof. Mustafa KARAMAN (Işık University)_____
(Thesis Supervisor)

Prof. Yorgo ISTEFANOPULOS (Işık University)_____

Prof. Nizamettin AYDIN (Yıldız Technical University) _____

Assoc. Prof. Uluğ BAYAZIT (Istanbul Technical University)_____

Assist. Prof. Ayhan BOZKURT (Sabancı University)_____

APPROVAL DATE: 08.06.2010

SOLID-STATE ARRAYS AND BEAMFORMERS FOR
SIDE-LOOKING INTRAVASCULAR ULTRASONIC IMAGING

Abstract

Current solid-state intravascular ultrasound (IVUS) devices use a one-dimensional (1-D) rectangular array wrapped around the cylindrical catheter. Beamforming in these devices is limited to synthetic phased array processing, and the image quality is degraded by low signal to noise ratio (SNR) and lack of focusing in elevation. We propose new solid-state reconfigurable cylindrical array configurations, based on non-uniform aperture sampling, enabling realization of low-cost integrated phased array beamformers based on the latest IC and transducer integration techniques. We employed non-uniform (Fresnel) aperture sampling with identical differential delays between adjacent elements to reduce dynamic beamformer complexity. For this purpose, the angles of the element boundaries and centers are determined by equalizing path difference of neighboring elements. For Side Looking-IVUS (SL-IVUS), the image plane is scanned through stepping the active aperture, and the active array must be reformed in each step. Fresnel sampled ring array leads to a simplified phased array beamformer with N/2 identical differential delays. The same logic applies to a two-dimensional (2-D) array with $N_L \times N_E$-elements over a cylindrical patch. We compared the proposed and existing array designs through numerical point spread function (PSF) simulations. The uniform and Fresnel sampled 1-D ring arrays perform similarly in terms of beam quality while the latter improves image SNR by a factor of $\sqrt{N_L}$ due to synthetic vs full phased array processing. The Fresnel sampled 2-D array performs dramatically better in elevation compared to 1-D ring array. The additional contribution of 2-D array on image quality is high SNR produced by phased array beamforming. The proposed Fresnel sampling of cylindrical aperture simplifies phased array beamformer by halving the required delay element count and transforms the complex 2-D beamformer into a separable beamformer that requires simple 1-D beamformers. The resulting 1-D and 2-D SL-IVUS array configurations could be realizable using monolithic integration of the analog beamformers with transducer arrays.

DAMARİÇİ YANABAKAN ULTRASONİK GÖRÜNTÜLEME İÇİN
STATİK DİZİ VE DEMETLEME DEVRESİ YAPILARI

Özet

Günümüzde kullanılan damar içi ultrasonik kateterler, statik kateterler, silindirik bir boyutlu (1-D) dizi yapıları kullanmaktadırlar. Bu yapılarda, derinlik yönünde dizi uzantısı olmadığından bu yönde demetleme yapılamaması ve yerleştirilen yüksek yoğunluklu dizi için gerekli kanal sayısı en temel problemlerdir. Artan kanal sayısı yapay dizi tekniğini kullanmayı zorunlu kılar ki bu teknik SNR değerini yükseltmektedir. Önerilen değişken boyutlu örneklenmiş (Fresnel örneklenmiş) statik dizi yapıları demetleme devrelerini basitleştirerek hem kateter üzerine iki boyutlu dizi yapıları yerleştirmeyi mümkün kılar hem de azalan kanal sayısı ile evreli dizi kullanılabilir. Fresnel örnekleme tekniği komşu elemanlara uygulanacak gecikme farklarının birbirinin aynısı olmasını sağlamalıdır ki bu gereken demetleme devresinin büyüklüğünü dramatik olarak düşürmektedir. B-scan görüntüsü elde etmek için silindirik dizi üzerinde bir alt-dizi seçilir ve lateral yönde kaydırılır. Her kaydırma adımında alt-dizi yeniden oluşturulmaktadır ve N/2 adet kanal kullanarak demetleme yapmaktadır. Aynı prensibi ikinci boyuta da uygularsak, kaydırılan 2-boyutlu (2-D) alt dizi $N_L/2 \times N_E/2$ kanal kullanacak ve ayrıca eksenel simetri sayesinde her eleman ile ilgili iki boyuta ait gecikmeler birbirinden ayrılabilecektir. Bahsedilen yöntemle elde edilen dizi yapıları, mevcut yapılar ile demetleme devreleri kompleksliği ve görüntü kaliteleri açısından numerik PSF benzetimleri kullanılarak karşılaştırılmıştır. Elde edilen sonuçlar Fresnel örneklenmiş dönüştürücüler ile tekdüze örneklenmiş dönüştürücülerin benzer sonuç verdiğini göstermiştir. Farklı olarak Fresnel örneklenmiş yapılar SNR seviyesini yükseltmektedir. Derinlik yönündeki dizi bu yöndeki çözünürlüğü ciddi bir biçimde iyileştirmiştir. Fresnel örnekleme bir yöndeki gecikme elemanı sayısını yarıya indirerek evreli demetleme elektroniğini basitleştirir, ayrıca 2-D dizide her eleman için her iki boyuttaki gecikme miktarının ayrıştırılabilir hale gelmesi 2-D demetleme devresinin basit 1-D demetleme devrelerinin birleşimi ile yapılabilmesini sağlar.

Acknowledgements

There are many people who helped to make my years at the graduate school most valuable. First, I thank Prof. Dr. Mustafa Karaman, my major professor and dissertation supervisor. Having the opportunity to work with her over the years was intellectually rewarding and fulfilling. I also thank Prof. Dr. F. Levent Değertekin who contributed much to the development of this research starting from the early stages of my dissertation work. I would also thank to the dean Prof. Dr. Yorgo Istefanopulos and the department head of electronics engineering Prof. Dr. Ahmet Aksen for their valuable advices.

Also I would like to thank to my graduate student colleagues who helped me all through the years full of class work and exams. My special thanks go to Ayça Şişman Aydın and Evrim Aydın for their valuable assistance. I am grateful for the support of Coşkun Tekeş whose friendship I deeply value.

The last words of thanks go to my parents. I would like to thank my parents Ayla and Necati Şişman for their patience and encouragement. Lastly I would like to thank my wife, Emine Şişman, for her valuable support.

This dissertation is dedicated to my little baby, whose existence has encouraged me…

Table of Contents

List of Tables

List of Figures

List of Symbols

$A(.)$	Aperture function
$b(.)$	Beamformed signal
$\Delta\tau$	The differential delay between adjacent transducer
f	Frequency
F	Focal distance
$h(.)$	Point spread function
$J_0(.)$	Zeroth order Bessel function
$J_1(.)$	First order Bessel function
K	Incompressibility
k	Wave number
λ	Wavelength
N	The number of transducers
R_f	Focal point
$\vec{n}$	Normal vector
$p(.)$	Excitation pulse
$PSF(.)$	Point spread function
R_f	Focal point
τ	Beamforming delay
$U(.)$	Observed field
v	Velocity

List of Abbreviations

1-D	One-dimensional
2-D	Two-dimensional
AA	Annular array
A-mode	Amplitude mode
B-mode	Brightness mode
C-mode	Contrast mode
CMUT	Capacitive micro-machined ultrasound transducer
DAA	Disk active aperture
DAA-2D-US	2 Dimensional disk active aperture uniform Sampled
DAA-2D-EFS	2 Dimensional disk active aperture elevational Fresnel sampled
DAA-2D-FS	2 Dimensional Rectangular active aperture–Fresnel sampled
FBW	Fractional band-width
FL IVUS	Front looking IVUS
IC	Integrated circuit
IVUS	Intravascular ultrasound
MHz	Megahertz
PSF	Point spread function
PZT	Piezo-electric transducer
RAA-1D	1 Dimensional rectangular active aperture
RAA-1D-FS	1 Dimensional rectangular active aperture Fresnel sampled
RAA-1D-US	1 Dimensional rectangular active aperture uniform sampled
RAA-2D	2 Dimensional rectangular active aperture
RAA-2D-EFS	2 Dimensional rectangular active aperture elevational Fresnel sampled
RAA-2D-FS	2 Dimensional rectangular active aperture Fresnel sampled

RAA-2D-US	2 Dimensional rectangular active aperture uniform sampled
SL-IVUS	Side Looking IVUS
SNR	Signal to Noise Ratio
ST	Single Transducer

Chapter 1
Introduction

Ultrasound is an extensively used technology due to its broad range of applications such as medical diagnostics, underwater exploration and nondestructive evaluation of materials. Ultrasound is a term used for sound waves having a frequency greater than 20 KHz, not sensible by human ear. The physical properties except its frequency are the same as audible frequencies. Ultrasound is commonly used for communication and navigation by bats, dolphins, and some other species in nature. The discovery of ultrasound goes back to 1790, when Lazzaro Spallanzani discovered that bats navigated with their ears, rather than their eyes in flight. Man made ultrasound devices dates back to 1920s. Ultrasound generated by man-made devices are used for imaging internal structures of the human body; to provide guidance in turbid deep sea waters; to map the ocean floor; for detecting flaws in airplane wings and nuclear power plant cooling pipes; for process monitoring in semiconductor manufacturing; for industrial cleaning and in many other applications. Hence, acoustics has a very broad range of applications in different frequencies and media. This study concentrates only on intravascular (IVUS) imaging applications using high-frequency sound.

1.1 Historical Review

Two breakthroughs in the 19th century in theoretical and experimental acoustics were the publication of The Theory of Sound by Lord Rayleigh in 1877, and the discovery of piezoelectric effect by the Pierre Curie and Jacques Curie in 1880, respectively. The piezoelectric effect has made it possible to generate and detect sound in megahertz frequency range. The invention of the vacuum tube at the turn of

the century allowed the development of ultrasonic instruments. The first ultrasound device is an echo sounding device called “hydrophone” launched by French physicist Paul Langévin and his coworker Russian electrical engineer Constantin Chilowsky on 1914.

First industrial implementation is in late 1920s for the flaw detection in metals. The device reconstructed acoustical waveform using light. The critical invention is pulse-echo dates back to 1940s. First medical applications of ultrasound were therapeutics, particularly tissue heating, because, the leading studies on ultrasound were focused on physical effects of it. The first use of ultrasound as a medical diagnostic tool was for imaging of brain tumors by Karl Thedore Dussik of Austria in the early 1940s. In 1949, sonic energy reflection from within soft tissue histological elements was reported by John Julian Wild, a surgeon, pioneering pulse-echo ultrasound imaging. J. J. Wild and John Reid, a newly graduated electrical engineer, put together the first ultrasonic scanning machine, and published the first paper on intensity-modulated cross-sectional medical ultrasonic imaging in 1952. The first real-time scanner was developed by Walter Krause and Richard Soldner and manufactured by Siemens Medical Systems of Germany in 1965. This product, called the Vidoson, used 3 rotating transducers housed in front of a parabolic mirror in water coupling system and produced 15 frames per second. Each frame consisted of 120 lines. The concept of the multi-element collimated linear electronic arrays was first described by Werner Buschmann in 1964. Early multi-element electronic beamformed device has launched by Acuson in 1983 offering excellent resolution and clarity at a low price. After the availability of powerful computer platforms in mid 1990s, the beamforming and signal processing stages in ultrasonic imaging systems have been realized in the digital domain. The quality of images produced by the ultrasonic imaging system has improved continuously due to advance in the ultrasonic transducer technology and microelectronics. The details of the history of ultrasound imaging and transducer technologies outlined can be found in several books [1,2] and papers [3-5].

1.2 Basic Principles

Sound waves propagate thorough a medium by vibration of molecules along the line of the transmitted wave. They are longitudinal waves with regions of compression

and rarefaction. However they may be expressed as sine waves with wavelength, frequency and velocity. The propagation velocity is constant in a homogeneous medium where wavelength is inversely proportional to frequency. The relation between these quantities is well known, $\lambda = fv$ where λ, f and v denote wavelength, frequency and sound velocity, respectively. The velocity dependency of propagating media is expressed as

$$v = \sqrt{\frac{K}{\rho}}, \tag{1.1}$$

where K is the incompressibility and ρ is the density.

The most common use of ultrasound imaging is pulse-echo. A basic representation is given in Figure 1.1. Here, firstly, the system is switched to transmitter mode and transducer is transmits the excitation pulse signal to the medium, then it is switched to receiver mode to get the reflected signal. The reflected signal carries information about impedance properties of the medium. The transducer converts the reflected pressure signal into an electrical signal, which can be converted to spatial information by multiplying with the sound velocity, assuming it is constant. The medium can be observed using the amplitudes of pulse-echo signals. That is referred to as the amplitude mode (A-mode) imaging.

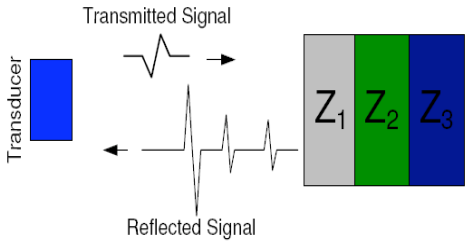

Figure 1.1 Pulse-echo imaging.

The ultrasound propagating in a medium goes thorough different medium dependent processes: reflection, refraction, scattering, and attenuation.

1.2.1 Ultrasonic Wave Propagation

The discontinuous or non-uniform media disturb the ultrasonic wave. In case of a

boundary, which is large compared to the wavelength, a portion of the wave is reflected and the remaining part goes through the boundary if the two media separated by the boundary are identical as shown in Figure 1.2(a). A different medium after the boundary changes the direction of wave; this is called refraction as illustrated in Figure 1.2(c). When the boundary is much smaller than the wavelength, uniform scattering occurs, which is illustrated in Figure 1.2(b). In case of boundaries with almost the same size as wavelength causes non-uniform scattering. The absorption of acoustic energy by the medium and diffraction results in attenuation.

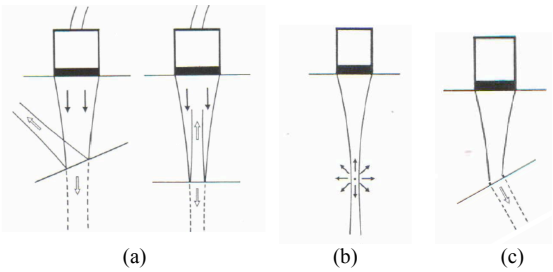

Figure 1.2 Ultrasonic wave and propagating medium interactions
(a) Reflection (b) Scattering (c) Refraction

Another wave phenomenon is diffraction, which is expressed by Huygens principle. The reflected wave from a boundary deviates, however this cannot be interpreted as reflection or refraction. The Huygens principle states that every point in an aperture or a surface, which reflects the wave, can be modeled as a source emitting ultrasonic waves. In order to determine the field intensity on a particular point, the effect of all individual point sources should be accumulated. The Huygens principle can be expressed mathematically as follows;

$$U_P(x,y) = \frac{1}{j\lambda}\iint_S A(x,y)\frac{e^{jk\rho}}{\rho}\cos\theta\, ds\,, \tag{1.2}$$

where U_P is the field intensity at point P, θ is the angle between the normal vector $\vec{n}$ and the vector pointing from point-source to observation point as shown in Figure 1.3. *A(x,y)*, aperture function, defines the source distribution along surface S and k is representing the wave number [6].

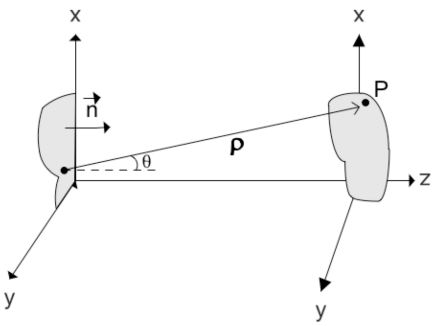

Figure 1.3 Diffraction geometry.

ρ can be expressed as follows,

$$\rho = \sqrt{z^2 + (x_s - x)^2 + (y_s - y)^2} = z\sqrt{1 + \frac{x_s^2}{z^2} + \frac{x^2}{z^2} - \frac{2x_s x}{z^2} + \frac{y_s^2}{z^2} + \frac{y^2}{z^2} - \frac{2y_s y}{z^2}}\,, \tag{1.3}$$

where (x,y,z) is the location of point P, and if it is far from the source ;

$$z >> x_s \;\;,\;\; z >> y_s \tag{1.4}$$

is satisfied and use the approximation, $\sqrt{1+u} \approx 1 + \frac{u}{2}$, therefore the expression can be simplified as,

$$\rho = z + \frac{x_s}{2z} + \frac{y_s}{2z} + \frac{x}{2z} + \frac{y}{2z} - x_s x - y_s y\,, \tag{1.5}$$

when we put ρ in to Equation 1.2,

$$U_P(x,y) = \frac{1}{j\lambda}\iint_S A(x_s,y_s)\frac{e^{jk(z+\frac{x_s}{2z}+\frac{y_s}{2z}+\frac{x}{2z}+\frac{y}{2z}-x_s x-y_s y)}}{z}ds \tag{1.6}$$

$$\Rightarrow U_P(x,y) = \frac{e^{jk(z+\frac{x^2}{2z}+\frac{y^2}{2z})}}{j\lambda z}\iint_S A(x_s,y_s)e^{jk(\frac{x_s^2}{2z}+\frac{y_s^2}{2z})}e^{jk(x_s x+y_s y)}\,ds \tag{1.7}$$

which is equivalent to the two dimensional Fourier transform of the product of the complex field of the radiating aperture and quadratic phase exponential.
Ignoring quadratic phase terms yields,

$$U_P(x,y) = \frac{e^{jk(z+\frac{x^2}{2z}+\frac{y^2}{2z})}}{j\lambda z}\iint_S A(x_s,y_s)e^{jk(x_s x+y_s y)}\,ds\,, \tag{1.8}$$

The resulting equation shows that the observed field at *P(x,y,z)* is the Fourier transform of the 2-D aperture shape *A(x,y)*. U_P gives the far field radiation pattern of aperture *A(x,y)*. It also determines the quality of generated beam by the aperture.

Wider aperture functions generate narrower beams, which should converge to a point. This radiation pattern is also called Point Spread Function (PSF) at far field. The assumption in Equation 1.4 is not valid for near field. Hence, PSF does not converge to Fourier transform of *A(x,y)* for near field, which is $\frac{D^2}{\lambda}$ distant from a flat circular aperture with a diameter of *D*.

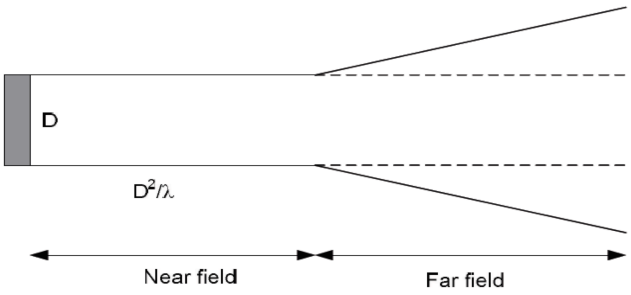

Figure 1.4 Approximated beam pattern of a flat circular aperture.

The case of flat aperture means it focuses on infinity, in other words all wave-fronts emitted by point sources on the aperture have the same phase at infinity. One can shape the aperture such that it focuses on a point other than infinity. Hence, the emitted waves have the same phase at that point. This enables the Fourier transform-PSF convergence also for mechanically focused apertures.

Chapter 2
Ultrasonic Imaging Systems

2.1 Overall System Architecture

Figure 2.1 illustrates the basic blocks of a simple ultrasonic imaging system. The area of interest is scanned by using a transducer array that uses pulse-echo. Transmit beamformer usually adjusts the transmit focus to half-depth of the imaging area. Echo signals collected by the array are beamformed according to scanning algorithm. The major types of scanning algorithms are given in Figure 2.2. Each beam represents an angle for sector scan or each beam can correspond to a linear distance. Signal and image processing unit converts the beamformed signal collection into image slices.

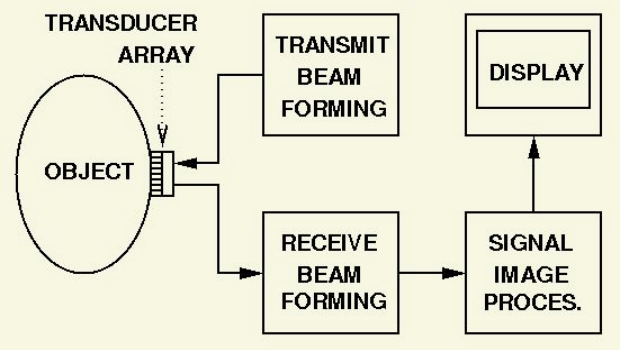

Figure 2.1 A basic block diagram of an ultrasonic imaging system

Early ultrasound imagers used to display A-mode images, in which just the amplified signals were monitored. Later, Brightness mode (B-mode) images were constructed by combining the pulse-echo signals received from each angle in order to form a 2-D image frame. Sector scanned B-mode slice is obtained as a function of scan angle and the depth. Here the depth is a function of time and is determined by dividing each received signal to ultrasound velocity. Contrast mode (C-mode) images are

independent of time since the ultrasonic beam is fixed at a certain angle. Hence the parameters of a 2D sector scanned C-scan frame are both angular. That results in a better imaging of moving objects for motion sensible application like valves in the hearth. Sector scanned B-mode or C-mode frames are first produced in 2D rectangular form. This slice format is scan-converted to standard Cartesian-coordinate video monitors. The scan conversion makes the image meaningful for operators.

Commonly used scan conversion algorithm is bilinear interpolation. Basically first xy space is sampled in order to obtain required resolution. Each xy sample's value is determined by the weighted contribution of 4 neighbor input samples. Figure 2.2(b) illustrates the process. S point is sampled point that has the coordinates, θ = arctg(y/x), $r=\sqrt{(x^2+y^2)}$. A(r_n, θ_n), B(r_n, θ_{n+1}), C(r_{n+1}, θ_n) and D(r_{n+1}, θ_{n+1}) are input values from image slice [7].

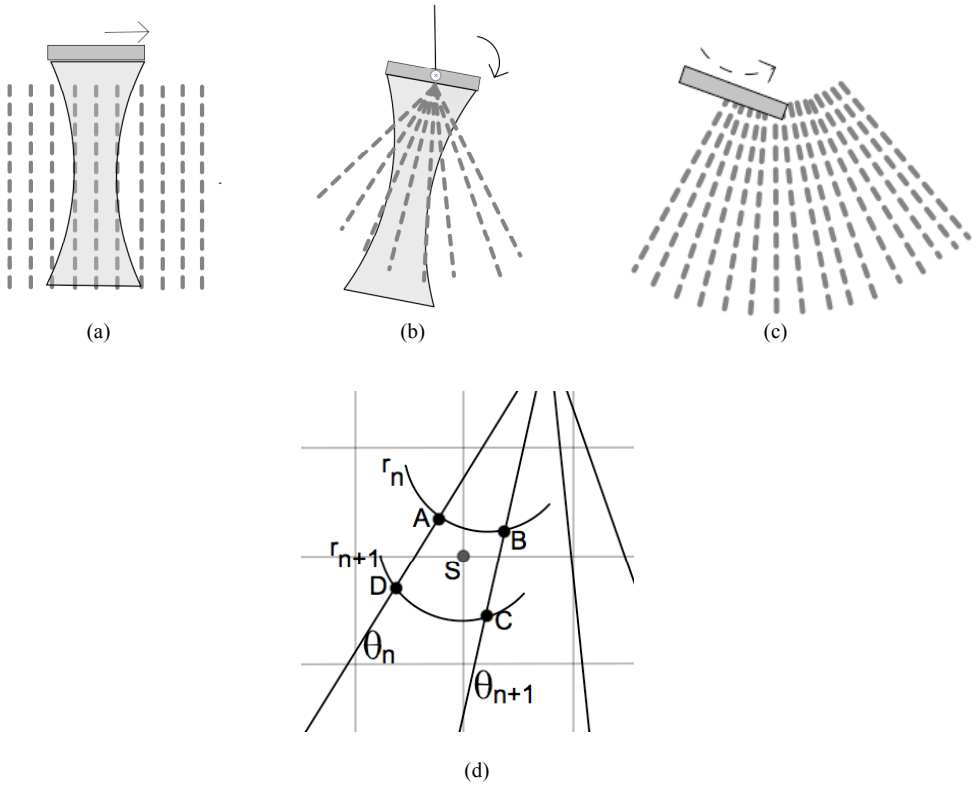

Figure 2.2 (a) Linear scanning (b) Sector scanning and (c) Arc scanning techniques (d) Illustrates the mapping of the bilinear interpolation illustration

2.2 Ultrasound Transducers

Ultrasound transducers convert the vibrations into electrical signal or vice versa. The electrical pulse applied to a piezoelectric material causes polarization, which leads to mechanical vibration. Some materials like quartz or barium titanate also produce electrical signals when they are vibrated. This phenomenon is known as the piezoelectric effect. Although Piezo technology is still extensively used in ultrasonic devices, technology has reached its limits in terms of size limitation, electronic integration and its bandwith. Latter technology is capacitive micro machined ultrasound transducer (CMUT) structures, which are promising as next generation ultrasound transducer.

CMUT structure has two electrodes; one buried in a silicon membrane and the other one placed on a silicon substrate as shown in Figure 2.3. A vacuumed gap is formed between the electrodes [8]. A vibration of membrane results in capacitance change, which can be detected by a voltage source. Inversely an applied voltage to electrodes causes mechanical vibration. Instead of using piezoelectricity, using CMUTs for generation and detection of acoustic waves has greater potential for electronic integration. This results in inexpensive integrated circuits for mass production and devices with increased noise immunity.

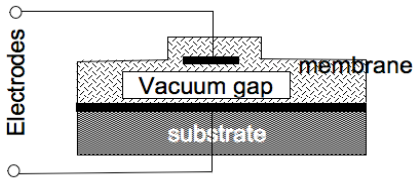

Figure 2.3 Single rectangular CMUT.

2.3 High Resolution Imaging Using Transducer Arrays

Aperture described in the Section 1.2.1 is actually a single transducer and its larger size results narrower beam, which improves the resolution. However, the large transducers cannot be implemented for many applications. Besides, the single transducer, which causes fixed focus or not focused operation, results in poor near-field resolution. Instead of using fixed focused operation, transducer can be sampled

in order to form a transducer array, which enables multiple focal zones by applying proper delays. Figure 2.4 illustrates mechanical and electronically focusing.

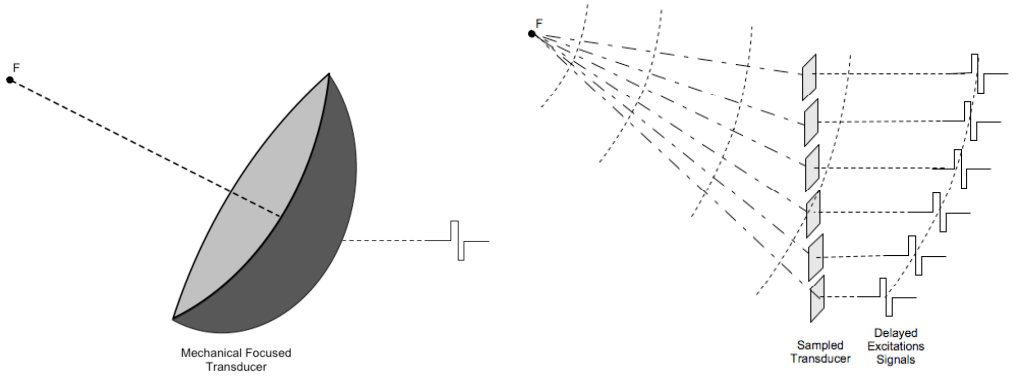

Figure 2.4 Mechanical focused single transducer and electronically focused sampled transducer.

2.3.1 Steering and Focusing

Transducer arrays using electronic steering and focusing improve overall quality significantly since they enable multiple focal zones. Applying proper delay profile may result focusing, steering or beamforming as shown in Figure 2.5. Beamforming is performed by applying steering and focusing together. A beamformer transmits or receives the acoustic signal to/from required angle and depth. It is mathematically expressed as;

$$b(t) = \sum_{N_j} \sum_{N_i} s(t - \tau_i - \tau_j - \frac{2F}{c}) \tag{2.1}$$

where *b(t)* is the beamformed signal, τ is beamforming delay applied for transmit and receive beamformers, F is the distance between array center and focal point [9]. Time delays of beamformer for the linear 1-D case can be calculated as,

$$\tau_i = \frac{1}{c}(\sqrt{(x_f - x_i)^2 + z_f^2} - F) \tag{2.2}$$

Here x_f and z_f are the coordinates of focal point and x_i is the coordinate of array element.

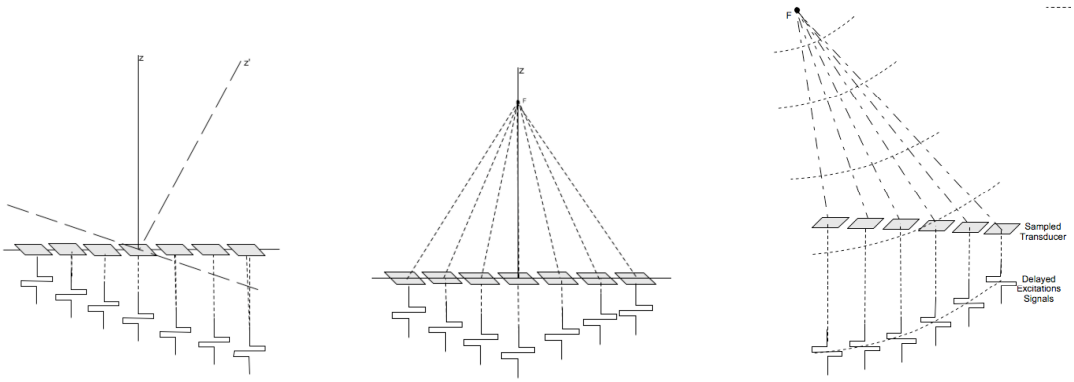

Figure 2.5 Steering, Focusing and beamforming illustrations

2.3.2 The Performance Measurement of a Transducer Array

In this section we will define the performance criteria of an array structure since it has serious effect on image quality. Assessing the performance of the array requires understanding the relationships between the characteristic of the system and the point spread function. Actually the plane to be imaged is the input of the array system and the output is the resulted image slice. PSF is the output of array system when the input is a point source. The point source is mathematically an impulse function hence the output of the array system must be the impulse response, which characterizes the system. In other words PSF is the spatial impulse response of the system, that is why system performance can be evaluated using PSF spatially.

For an array of transducer elements (sampled transducer aperture) the PSF is expressed as,

$$U_P = \sum_{N_x} \sum_{N_y} A(n_x, n_y) e^{jk\rho}$$

For instance, the PSF function for N element 1-D linear array with size D can be determined as,

$$U_P = \sum_{N} e^{jk\rho} \tag{2.3}$$

$$\rho = \sqrt{(\frac{nD}{N} - \frac{D}{2})^2 + z^2 + az(\frac{nD}{N} - \frac{D}{2})\sin\theta} \approx z + \frac{n^2 D^2}{2z} + \frac{nD}{N}\lambda u \qquad (2.4)$$

where u is $\frac{\sin\theta}{\lambda}$. Ignoring quadratic phase terms and substituting ρ in Equation 2.3 yields,

$$PSF(u) = e^{jkz}\sum_{N} e^{jk\frac{nD}{N}\lambda u}, \quad d \triangleq \frac{D}{N} \qquad (2.5)$$

Resulting PSF is,

$$\frac{\sin(N\pi du)}{\sin(\pi du)} \qquad (2.6)$$

Here each array element is assumed as a point source. For the parameters, N=8 and d=1.5λ, the resulted PSF is shown in Figure 2.7 [10]. There is grating lobes at $sin\theta$ = 0.72 and sinθ = -0.72, resulting poor image resolution laterally. The grating lobes are not visible when the element pitch (transducer sampling) is greater than 0.5λ and no steering is applied; otherwise they degrade the image quality. Another important indicator of image resolution is main-lobe width, which are the beamwidths at 3 dB, 6 dB or 20 dB. Here 3 and 6 dB values represent half-power beamwidths for one way and two-way responses respectively; 20 dB is the width at which the main-lobe intersects the horizontal axis. This value is proportional to λ/D where D is the aperture width. Since wavelength is decreased as operating frequency is increasing narrower beam width is obtained at high frequency systems. The side-lobe levels of PSF function also affect the contrast of the image. Side-lobe levels depend on transducer distribution of aperture, the weighted function if it is applied and focusing capability of the array. Consequently as expected, PSF function exhibits the important performance criteria about the imaging system.

We considered grating lobes, main-lobe width, and side-lobe levels using PSF. They impose contrast and pixel resolution of the image. Additionally image quality is also affected by temporal resolution, which depends on the bandwidth excitation pulse and axial response of the transducer array. The physical length of the ultrasound pulse should be less than ½ of required axial distance of adjacent image pixel in order to avoid overlap. It is illustrated in Figure 2.8.

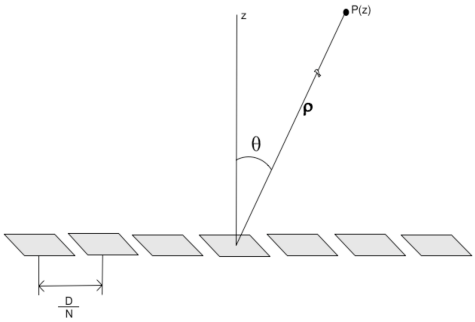

Figure 2.6 Geometry for PSF derivation

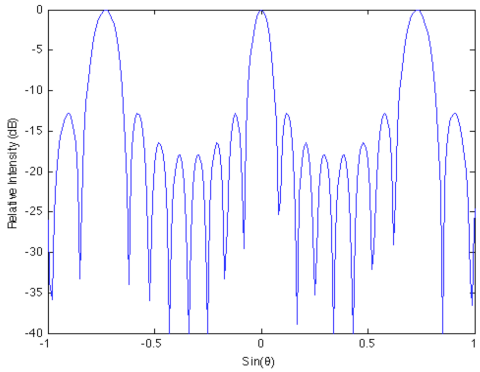

Figure 2.7 PSF function for linear 8-element array with element pitch of 1.5λ

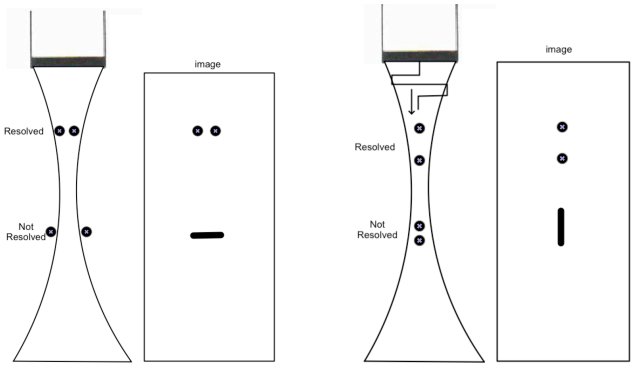

Figure 2.8 Lateral and axial resolution illustrations

2.4 Beamforming Techniques

Research studies on ultrasonic technology have aimed to improve image quality. The frequency range is limited by sensor technology, and the array size is constrained by the physical requirements of the application. Hence many cases allow only relocation of transducers, employing weighting functions or large aperture synthesis using small sized subapertures and multiple firings in forming a single image frame. Various imaging techniques have been developed aiming to improve image quality for different applications. The beamforming techniques are summarized using Ultrasound Imaging Vol I, Section 1.4 [7] and the papers [11,12].

2.4.1 Full Phased Array

Phased array is a widely used imaging technique. In the full phased array, all elements are activated simultaneously to generate the required beam. Each element

must have its own channel hence proper delay is applied. However the technique requires excessive number of channels, therefore it is difficult to implement for small-scale applications. Since all array elements are activated simultaneously, the SNR value is higher.

2.4.2 Classical Synthetic Aperture

Classical synthetic aperture may have just one moving transducer or may use one stepping element in a transducer array. Beamforming is realized using saved A-scan set. Either moving transducer or stepping element simplifies the implementation since each frame can be obtained only using N A-scans. However insufficient number of A-scans result in poor SNR and high sidelobe levels. Additionally the structure is sensitive to motion due to acquisition time of an A-scans set.

2.4.3 Synthetic Phased Array

Unlike the classical case, in this technique a sub-group of elements is activated requiring more resources. Comparatively, synthetic phased array improves the SNR, decreases susceptibility to motion and causes better resolution. Basically the technique is a trade-off between front-end electronics complexity and image quality.

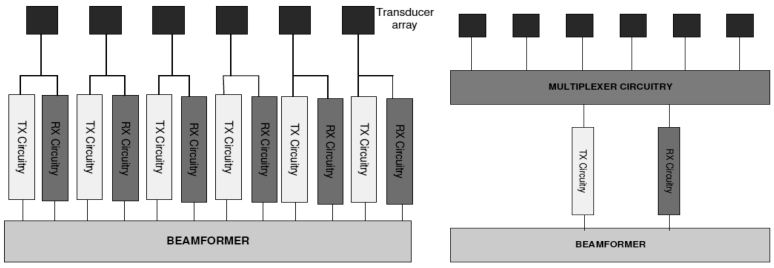

Figure 2.9 Phased array beamforming and classical synthetic phased aperture front-end electronics block schemes

2.5 Beamformer Types

Gold standard beamformer can drive the phased array in both transmit and receive mode; and the beamformer's mathematical expression can be expressed as given in Equation 2.1, where it is considered that there is no limitation originated by front-end

electronics and frame construction time assumed to be enough. These constraints require some limitations of beamforming like fixed transmit focusing, resulting in poorer resolution.

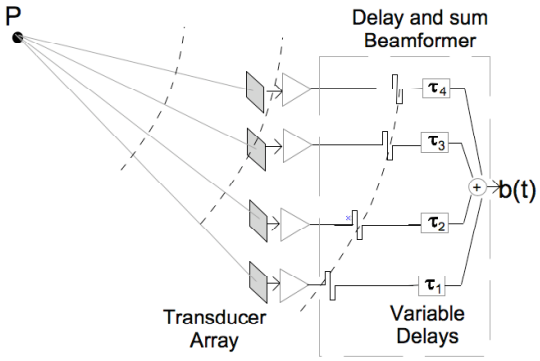

Figure 2.10 Basic schema of delay and sum beamformer

Two classifications of beamformer types are possible;

1) RF vs Base band beamformer;
2) Analog vs Digital Beamformer.

RF beamforming is easy to implement using a simple hardware. Beamformer directly delays each A-scan. However each delay must be precisely quantized in order to minimize quantization effect on constructed image. Although base-band beamforming does not need to be that precise, the requirement of complex hardware is a major drawback. The signal is first shifted to baseband by mixing an intermediate frequency sinusoidal wave. A low-pass filter selects baseband then both in-phase and quadrate channels are delayed by time and phase delays.

Early systems have utilized analog delay lines to implement beamformers. Employed inductor-capacitor ladders result in inaccurate delays due to the dependency of minimum delay value. Additionally, it cannot be implemented for large number channels. The advances in IC technology enabled digital beamformers in late 1980s. Digital systems enable large scale array processing but limited number of cables constraint of same applications requires analog beamformation. Hence many hybrid system designs are available.

2.6 Array Structures

Early ultrasonic system uses one focused or unfocused transducer employing mechanical scanning. Further developments in transducer and IC technology enable electronically controllable array systems, which lead to new practical applications and increase the system quality. Here we describe the generic array geometries used in ultrasound area. The geometries are shown in Figure 2.11.

Even though their limited imaging capabilities, 1-Dimensional arrays are still in use due to simplicity of their front-end electronics. Only one-directional focusing is possible therefore they can only be used for 2D imaging. For many applications like IVUS or ICE, 3-D scanning is essential, however 3D imaging requires 2-D array, which has excessive number of channels. Many synthetic beamformer techniques and 2D array geometries are proposed to reduce the channel size. 2D planar arrays might be practical when using effective synthetic phased array imaging techniques. Another way of reducing the number of channels is using a planar array, in which element locations are randomized or not uniform. Using this method, reasonable designs can be accomplished under the constraint of reduced side-lobe level.

Annular arrays are another configuration, providing high-quality axially symmetric beams. The axial symmetry eliminates the capability of steering electronically; annular arrays might only focus on different depths. That is why annular arrays can be classified as 1.5D arrays and they must be mechanically steered.

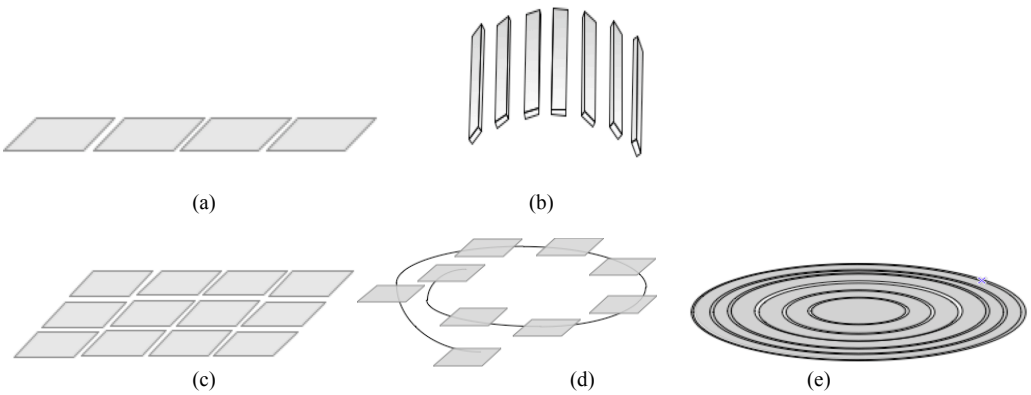

Figure 2.11 Generic array structures, (a) 1-D planar array. (b) 1-D cylindrical array. (c) 2-D planar rectangular array. (d) Spiral-planar array (e) Annular array

Chapter 3
Intravascular Ultrasound

Although contrast angiography is applied widely for both diagnostic and therapeutic purposes today, it has some serious weaknesses. For example, it is impossible to define the lesion type, 3-D visualization is not possible, lesion dimensions cannot be guessed precisely and the visualization of circumference of the vessel wall is not possible [13]. IVUS technology enables real-time, cross-sectional in-vivo images of arteries aiding in the diagnosis of arterial diseases and providing information on vascular pathologies such as plaque structure and lesion type [14]. Image examples obtained by an IVUS probe is illustrated in Figure 3.1.

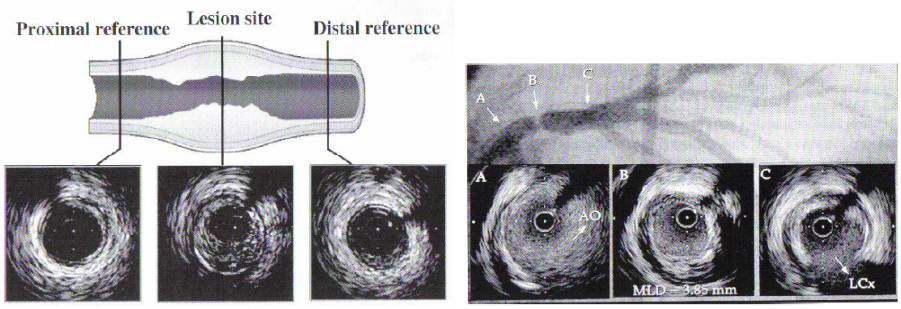

Figure 3.1 (a) The lesion site can be seen easily since it causes considerable change of vessel diameter. The lesion size can be measured using this difference. (b) The images obtained by angiography and IVUS can be compared. Lesion is pointed by 'B' [14].

IVUS probes are also used as guiding apparatus for intravenous operations like stent deployment and balloon angiography. Repeated IVUS investigations allow tracking the natural course of atherosclerotic lesions and effects of therapeutic measures such as lipid-lowering therapy [15,16].

Since IVUS probes operate in small and tiny vessels, they must be as small as1 mm. That seriously affects image quality due to difficult array and front-end electronics integration in such a small area. Another limitation is piezoelectric transducer

technology, which form the basis of current IVUS probes. PZT limits the operation frequency, bandwidth and the technology leads fabrication problems for small-scaled array systems. In addition to fabrication problems, which increase catheter cost, piezoelectric transducers cannot be directly integrated with silicon integrated circuits (IC) to realize IVUS arrays with smaller dimensions. In contrast, micromachined transducers enable both low-cost, low-profile, and advanced IVUS probes. CMUTs have manufacturing and performance advantages over piezoelectric transducers especially for imaging arrays with small dimensions [17,18].

Two different IVUS probe structures, which are classified according to their beam direction, have been introduced. The beam generated by forward looking IVUS probe illuminates the forward direction as its name implies. SL-IVUS enables the imaging along the lateral cross-section of catheter by illuminating this area. Mostly, these two architectures are not alternative of each other since both of them have unique advantages and application areas.

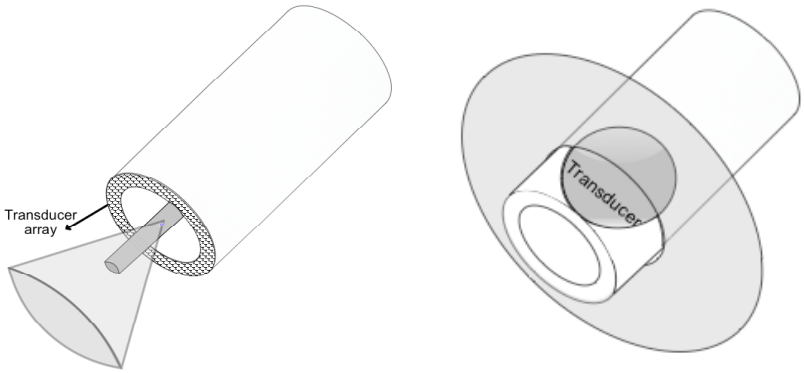

Figure 3.2 Illustrations of ring-array forward looking probe and rotating transducer side looking probe

3.1 Forward-Looking IVUS

The need of FL IVUS has arisen due to the guiding deficiency of SL-IVUS systems. However FL IVUS probe also has unique advantages for instance it illuminates the volume perpendicular to blood flow direction, enabling blood-flow imaging. Additionally FL IVUS probe has the potential of 3-D, real-time imaging. However, required number of channels causes fabrication difficulties, which motivates new designs enabling fabrication A ring array mounted on the catheter tip is illustrated in

Figure 3.2. Fabrication difficulties disable integrated beamformer, which results using synthetic array imaging. As mentioned in chapter 2, the synthetic imaging technique causes poor SNR and increases the sensitivity to tissue motion. Hence the number of channels should be optimized.

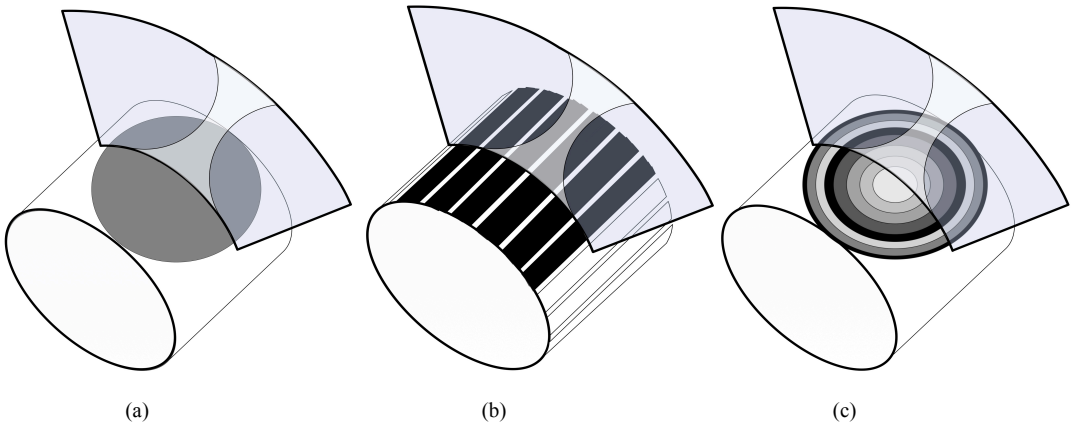

Figure 3.3 The illustrations of existing SL-IVUS structures, generated beams and B-scan cross-sections, (a) Fixed focus single transducer, (b) Solid-state uniform-sampled high-density array, Electronically rotating Active-Aperture is indicated by black, (c) Equal-area concentric annular array

3.2 Side-Looking IVUS

The dissertation is focused to SL-IVUS imaging. SL-IVUS probes are revolutionary for invasive vascular operations. They are applicable for not only diagnosis purposes but also therapeutic operations or they can be used as guiding tool. SL-IVUS probe can measure vessel/lumen diameter, lesion length and helps to determine the amount of plaque buildup in a vessel and its composition. It is useful especially when the 2-D images of conventional angiography are unreliable; such as the imaging of the regions with multiple overlapping arterial segments. It is also used to guide in stent deployment and balloon angiography operations for accurate placement. Besides, SL-IVUS probe potentially helps to identify vulnerable plaque and the analysis of plaque structure, which is called as virtual histology. The main defect of SL-IVUS probes is guidance problem. That is why they are guided using contrast angiography, however forward looking probes are proposed to overcome the guidance problem. Another problem is poor image resolution causing interpretation difficulties of

obtained image. The array performance criteria, mentioned in Chapter 2, should be optimized in order to improve resolution. This dissertation introduces two new SL-IVUS probe structures explored by numerical computer simulations and experimental studies. First we introduce the existing SL-architectures:

3.2.1 Rotating Single Transducer

The first practical IVUS scanner utilizes a rotating single transducer, which is disk-shaped or rectangular. Combining the A-scans collected from each angle simply forms the B-scan image since each A-scan carries information about the impedance differences of corresponding angle [19]. The single transducer, uses the side surface of the catheter effectively. Transducer size is almost the same as the probe diameter as shown in Figure 3.3. Larger probe size improves pixel resolution, however single unfocused transducer causes poor lateral resolution due to high side-lobes. Usually the transducer is mechanically focused to the half of image depth that results in great resolution at that depth whereas out of the focal zone the resolution is poor. Another drawback is mechanical rotation, which leads to axial movement that worsens the image quality. Some synthetic aperture studies are aimed to obtain improved resolution but synthetic aperture results in higher sidelobes. There is a trade-off between low sidelobes and narrower beam out of focus [20-22]. We will use fixed focused circular structure for simulations in Chapter 4.

3.2.2 Solid-State Array

Latter approach is employing a solid-state array that solves the fixed focusing operation problem and mechanical distortions by employing a circumferential array. High-density array is wrapped around the catheter; a 90-degree sub-array (sub-aperture) is stepped electronically to scan the area of interest. Active aperture is indicated by black in Figure 3.3. The rotating active-aperture requires large number of parallel channels, which makes the integrated beam former impossible. Therefore the solid-state structure enforces the use of synthetic aperture imaging leading to degraded SNR. Another origin of poor SNR is small size of transducers due to their high impedance. Besides, high saggital asymmetry in imaged lesion leads additional

distortion because the array has no elevational extension to improve image thickness performance.

The main design consideration of high-density cylindrical array is the received acoustic power. Limited transducer size increases the impedance resulting weak signal detection. Lateral length of the transducer is limited by catheter diameter. The length in elevation is determined according to focal depth and the impedance constraints. Since lateral size is limited, elevation size should be larger to obtain small impedance, which makes the low-noise amplifier easier. However, in order to prevent destructive interference the difference between two distances, axial point at focal depth to the center and to the edge of the transducer, should be less than 0.5λ [23].

A realizable 32-element circular array design, employing synthetic aperture imaging and an optimal filter to improve SNR, are introduced by O'Donnell *et al*. in [24]. Shapo and O'Donnell fabricated a 1.2 mm-diameter, 20 MHz high-density circular array including 32 elements. The tests showed that satisfying synthetic aperture images could be produced if the circular array and the optimal filter are combined [25]. Image quality was greatly improved using 64-element, high-performance, 20 MHz ceramic array constructed by O'Donnell *et al.* in [26]. The reported experimental results are promising for not only in diagnosis applications but also in blood flow imaging and stent deployment. An unconsidered drawback of 1-D circular array is the degraded image quality due to the lack of elevational focusing. This leads to a very poor resolution in that dimension.

3.2.3 Annular Array

We have explored usage of annular array for side looking IVUS. Our study is presented in Chapter 4. Here we mention about the advantages of annular array and the recent research about it.

Annular array combines the high-bandwidth and satisfactory SNR of large elements and the capability of multiple focal zones. Figure 3.3-c illustrates annular array structure. The axial symmetry of annular shape improves the beam quality and

reduces the required number of channels, which simplifies front-end electronics complexity, however this symmetry requires mechanical scanning to form an image frame. Designs based on equal-width and equal-area elements have been explored in recent studies. Equal width design obtains better near-field performance whereas the commonly used equal area design provides both maximum axial pressure and simplified beamformer. Hazard *et al*. have performed detailed PSF simulations on equal width configuration and reported that 20-element imaging performances of annular array and 128-element linear array are similar [27]. Brown *et al*. have described all steps of designing an equal-area annular array and they fabricated a miniaturized 2-mm.-diameter PZT annular array operating at 50MHz with FBW 52% [28]. Further miniaturized equal-area, 840-μm-diameter array operating at 50 MHz with FBW 40% has recently demonstrated [29]. These studies show that annular array designs are satisfactory in terms of lateral end elevational beam performance, but the need of mechanical scanning leads serious fabrication difficulties and results distortions in the reconstructed image.

Chapter 4

Intravascular Ultrasound Imaging Using Annular array

This chapter explores a new proposed rotating annular array for SL-IVUS probes. The study involves detailed comparison of existing structures and rotating annular array. The simulations were verified using analytical derived PSFs and they were also validated by experimental data. Experimental studies were realized by a custom designed annular array employing capacitive micro machined ultrasonic transducer CMUT technology. CMUT technology is suitable for electronic integration due to its silicon-based fabrication process. Electronics integration helps not only with miniaturization of the probe but also improves signal quality by minimizing the parasitic capacitance.

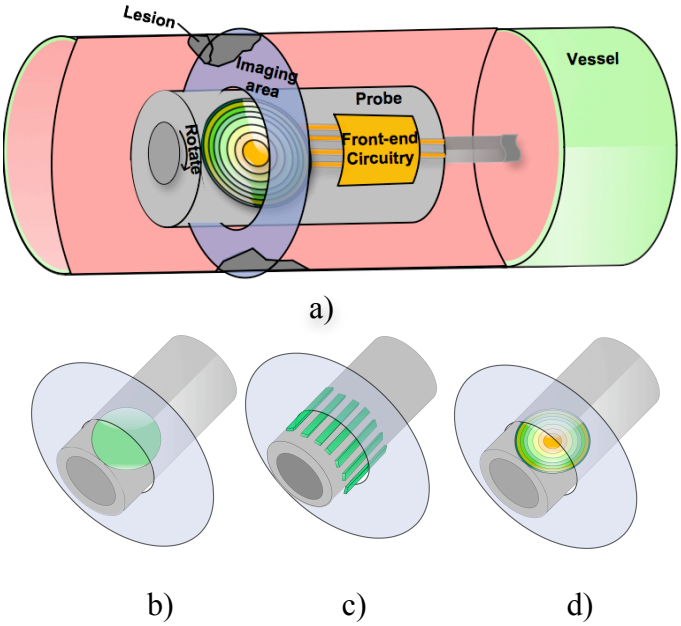

Figure 4.1. a) The shematic of SL-IVUS probe and the 2D cross-section to be imaged presented. b) Rotating single transducer. c) Solit state array d) Rotating phased annular array.

Since image resolution is an important aspect of the utility of IVUS, improving image quality without compromising proper IVUS probe size and front-end complexity can have significant impact on this technology. Current practical PZT-array structure requires complex fabrication process which limits the operation frequency to about 20 MHz with 20-30% FBW. Excessive number of firings in synthetic aperture data acquisition in these probes increases susceptibility to tissue-catheter motion artifact. Furthermore, PZT-arrays with many elements may increase catheter cost since they cannot be directly integrated with silicon integrated circuits. Annular arrays provide another probe structure for SL-IVUS as shown in Figure 4.1(a). In an annular array smaller number of elements can produce the same quality beam compared to a focused single element. Decreased element number allows bigger element size yielding improved SNR and point resolution. Many piezoelectric annular array designs are reported of which the smallest has 2mm diameter and 50-MHz operating frequency at 52% FBW [29-30].

4.1 Simulated Point Spread Functions

This section will explore rotating annular array structure through simulations. We tested the array performance using two-way Point Spread Functions. Following simplified expression was used in our computations,

$$h(r) = \overbrace{\sum_{\underbrace{n=1}_{Elements}}^{N} \sum_{\underbrace{i=1}_{Samples}}^{K}}^{Transmit} \overbrace{\sum_{\underbrace{m=1}_{Elements}}^{N} \sum_{\underbrace{j=1}_{Samples}}^{K}}^{\text{Receive}} \overbrace{\cos\varphi_n \cos\varphi_m}^{Directivity} \overbrace{p\left(\frac{2|r|}{c_0} - \tau_n - \tau_m - t_i - t_j\right)}^{Excitation\ \ Pulse} \qquad (4.1)$$

where *h(.)* is the PSF; *r* is the vector representing the observation point; *p(.)* is the excitation Gaussian pulse; c_0 is the ultrasound velocity; t_i is the flight time between i^{th} element and the point target; τ_i is the focusing delay time. Angular response of each transducer is modeled using cosine function; φ_n is the angle with respect to n^{th} element normal. Receive mode f-number apodization is applied for the ranges smaller than *f*/2. Receiver array was narrowed as the focused range reduces. For instance receiver array is halved when receive focus is set to *f*/1.

We also computed the approximated (far-field, continuous wave) theoretical two-way (transmit-receive) PSFs of Annular array and solid state array which are expressed as;

$$PSF_{AA}(\theta) = \sum_i \frac{r'}{k\sin\theta} J_1(kr'\sin\theta)\Big|_{r'=a_i}^{b_i} \tag{4.2}$$

and ,

$$PSF_{ss}(\theta) = \pi R^2 \frac{J_1(kR\sin\theta)}{kR\sin\theta} \tag{4.3}$$

where PSF(θ) is point spread function, $J_1(.)$ is the first order Bessel function; θ is the lateral angle measured from the array axis; λ is the wavelength. Note that inner and outer radii of the i^{th} element are a_i and b_i, respectively.

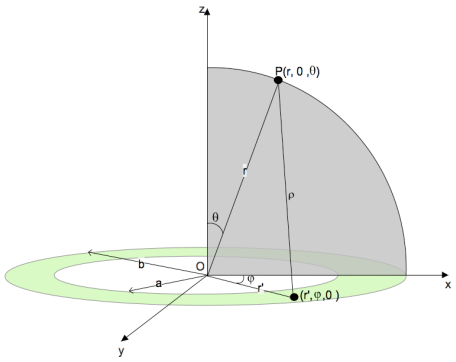

Figure 4.2 Geometry for annulus beam calculation.

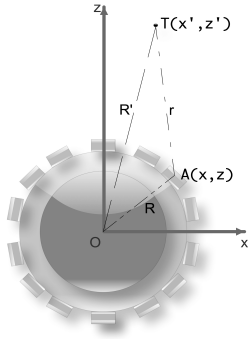

Figure 4.3 Geometry for solid-state beam calculation.

The derivations are calculated using geometries in Figure 4.2 and Figure 4.3

We tested the simulation studies by running the simulation for far field, continuous wave case. We plotted the simulated and analytic derived results in the same plot. Figure 4.4 and Figure 4.5 are for annular array and solid-state geometries. Figures show both of annular array and solid state geometries fitted well.

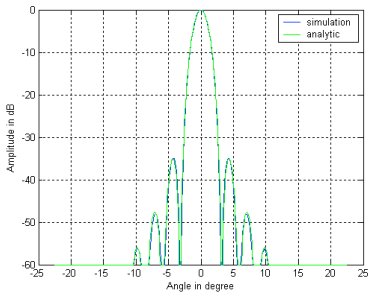

Figure 4.4 The verification of annular array simulation.

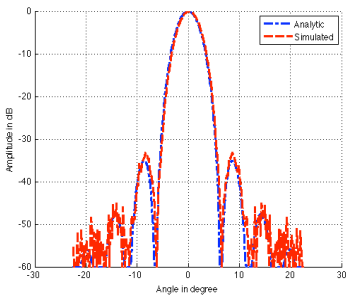

Figure 4.5 The verification of solid-state array simulation.

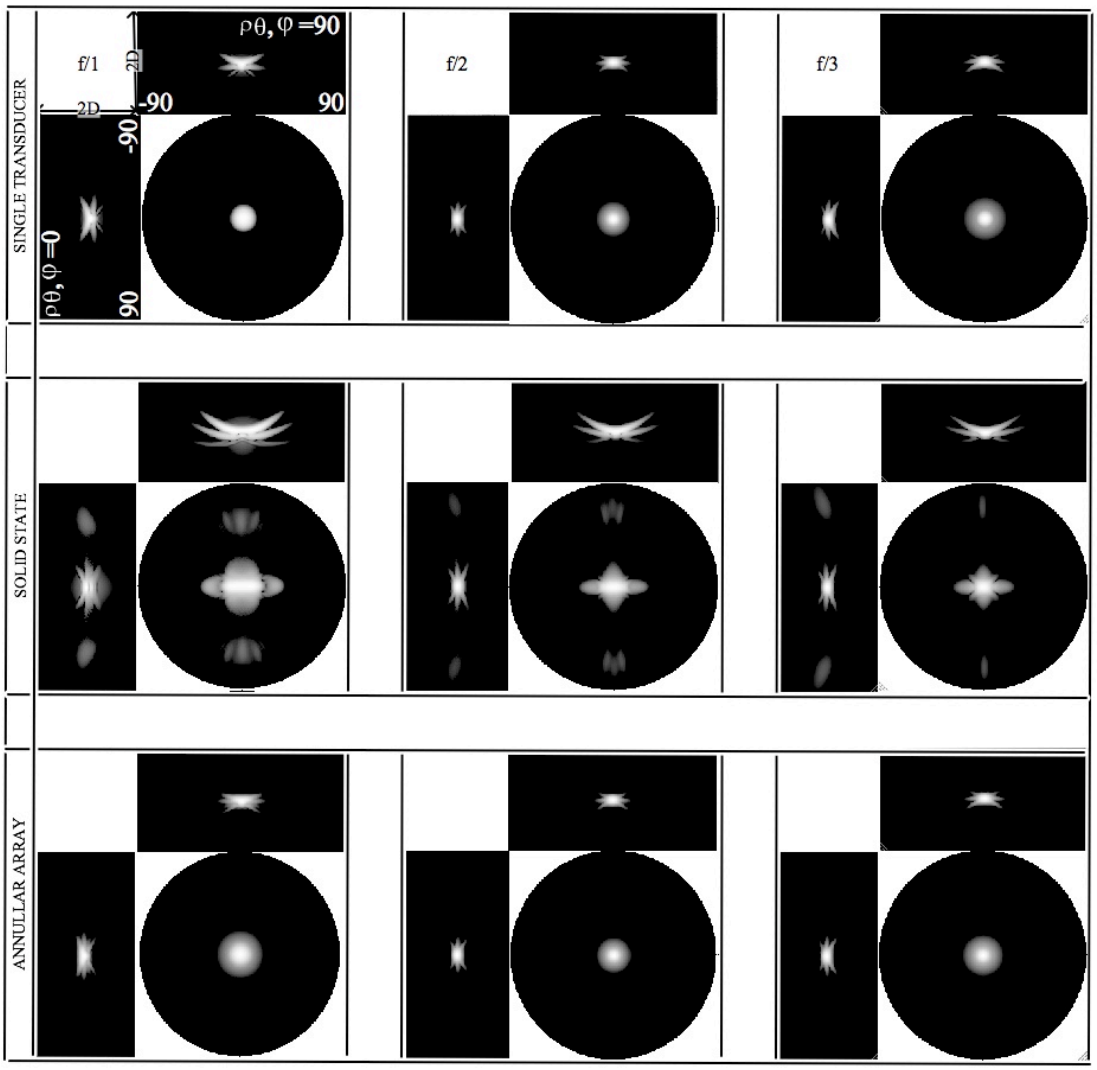

Figure 4.6 Beam patterns of existing probe types are illustrated with a dynamic display range of 50 dB. Constant ρ, elevational and lateral cross-sections for single transducer (ST), solid-state (SS) and annular array (AA) structures are presented at ranges *f*/1, *f*/2 and *f*/3.

The simulation parameters of different array types are chosen to enable fair comparison. Catheter radius is 420 μm, Aperture size is 600 μm for each case; we used a 20 MHz Gaussian pulse with 65% bandwidth. Numerical computer simulations are performed using three on axis point targets at ranges *f*/1,*f*/2 and *f*/3. Single transducer has fixed focus operation at *f*/2; solid-state and annular array enable dynamic focusing hence receive dynamic focusing is used for these cases, however their transmit focuses are also set to *f*/2. The results are presented in Figure 4.6. For ease of investigation 1D plots are given in Figure 4.8. Figure 4.6 shows that the single transducer structure has wider beams at ranges out of focal zone because of fixed focus operation. Its beam around focal point performs the best of such size

array, and it is illustrated by PSF at range *f*/2. Single transducer and annular array provide the same focal zone performance, however annular array has dynamic focusing capability, which results narrower beam at ranges *f*/1 and *f*/3.

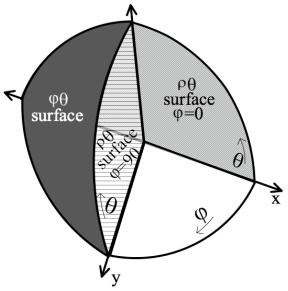

Figure 4.7 Simulated φθ, lateral-ρθ and elevational-ρθ surfaces.

Although solid-state also enables dynamic focusing the beam at focal range *f*/2 is wider due to poor acceptance angle. Although we use the same active aperture, directivity factor, cosφ in Equation 4.4 causes wider beam in solid-state case. Solid-state structure has narrower beam at *f*/1 since its sampling enables precise f# apodization. Elevation beam of solid-state structure is extremely wide due to the absence of elevational array extension. Single transducer and annular array have the same elevational and lateral beams because of their axial symmetry. Averaged 1-D plots enable quantitative investigation and they are illustrated in Figure 4.8. Elevation 6-dB beamwidth of Solid-state structure is measured as 26°, 14°, 8.7° at ranges *f*/1, *f*/2 and *f*/3. In contrast annular improves these values by about 16°, 7°, and 2.2°. Solid-state structure is wider about 1° laterally and it has a grating lobe under 40 dB, nevertheless, lateral differences are ignorable. The leading disadvantages of Solid-state structure are the lack of poor elevation beam and low SNR limited by synthetic aperture imaging.

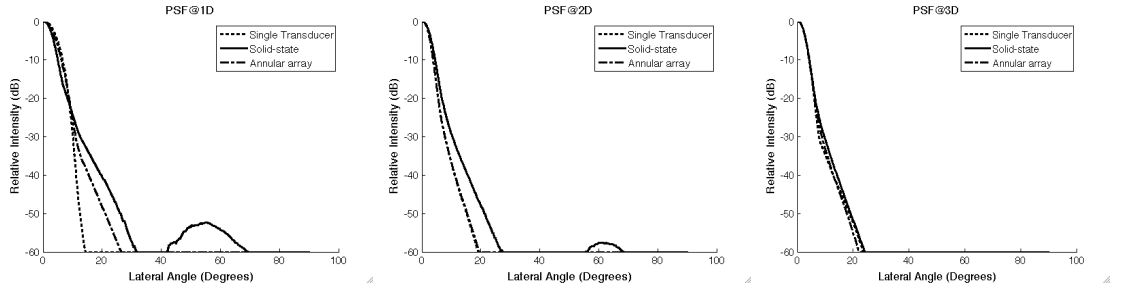

(a)

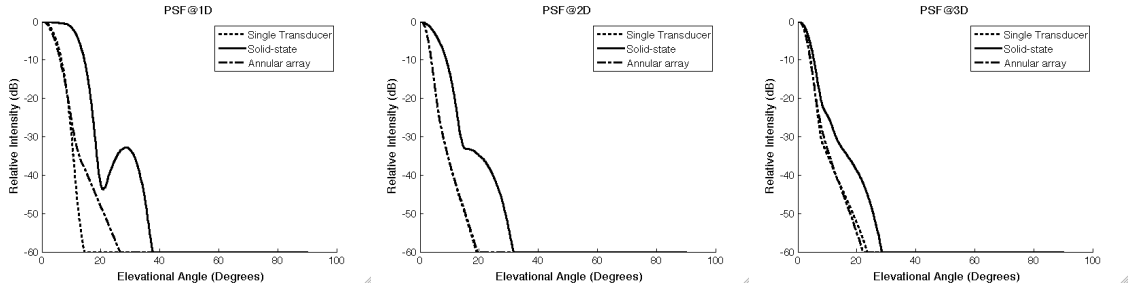

(b)

Figure 4.8 (a) Lateral and (b) Elevational Cross-sectional images of beam pattern for existing probe structures and rotating annular array.

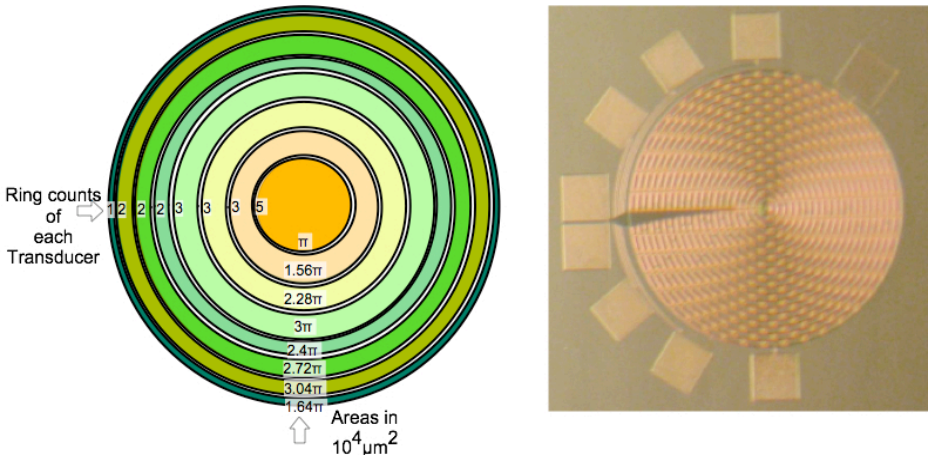

a) b)

Figure 4.9 a) Designed annular array's parameters. b) Fabricated annular array.

4.2 Design Considerations

An SL-IVUS probe architecture that has a rotating annular array is schematically shown in Figure 4.9(a). Since annular array produces axisymmetric beams, focusing

is achieved only along its axis. Therefore the annular array should be rotated mechanically to obtain 2-D cross-sectional images.

Although the array is capable of dynamic transmit and receive focusing, only dynamic receive focusing is employed otherwise excessive number of firing is needed. The transmit focus provides the flexibility of having different transmit depths in successive frames.

Here IVUS applications allowing a catheter with 1-mm. in diameter is considered, therefore the designed and fabricated structure is a 0.84-mm diameter annular array, which consists of 8 concentric similar-area CMUT transducer elements. Annulus has 21 ring-shaped 18-μm wide CMUT membranes separated by 2 μm. The rings are connected to each other to form similar area transducers as indicated in Figure 4.9(b).

4.3 Experimental Results

The fabrication of two annular arrays operating at 20 MHz and 50 MHz frequencies are completed. Each array was wire bonded to a chip carrier. This chip holder was inserted into a ZIF socket on a custom PCB with a pulser based on an RF power MOSFET (DE150-501N04A), a receiver based on low-noise transimpedance amplifier (AD8015) and switching capabilities. Due to the limitations of the electronics, neighboring annular element pairs (total of seven) were used as transmits and receive elements, also known as pitch-catch mode.

The experimental setups shown in Figure 4.10(a) and Figure 4.10(b) were used to collect data using the two arrays in linear scan mode. The reconstructed B-scan images are presented in Figure 4.11. Here we also present 1-D lateral cross-sectional plots of the experimental and simulated PSFs.

We first examined the received signal amplitudes and SNR for each a-scans. In order to calculate SNR, the RMS value of the noise is calculated from a section of data without any acoustic signal whereas the signal amplitude was taken as the RMS of the signal in time window covering the echo pulse.

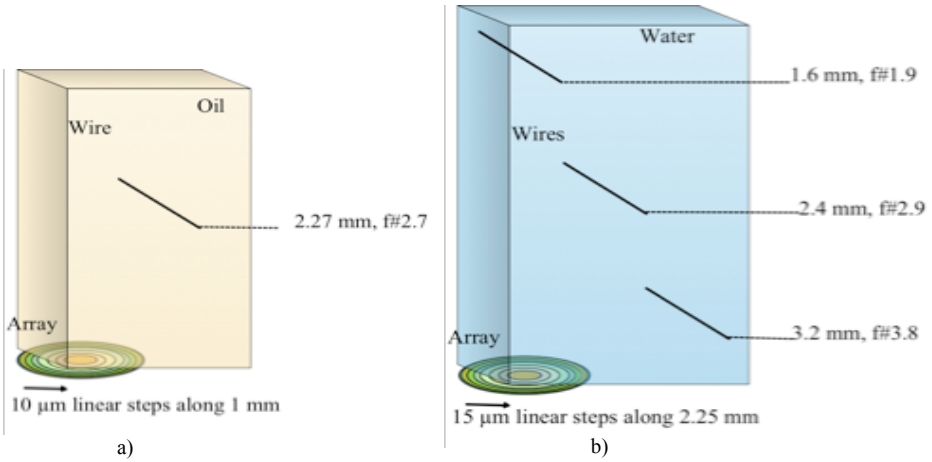

Figure 4.10 a) 20 MHz array experimental setup, wire target is at f/2.7, 100 linear, 10 µm step is used for scanning. b) 3 wire targets is used to test 50 MHz array, step interval is 15µm. count is 150.

The range of SNR echo signals is between 12 dB-22 dB. This variation is mostly due to the element area. The range of SNR of 20MHz echo signals is between 21 dB and 33 dB. The 6 dB fractional spectrum was corrected for diffraction and attenuation neither water nor oil. The 6-dB main-lobe beamwidths are measured as 250 and 120 µm. and they are close to simulated, 255µm and 116 µm.

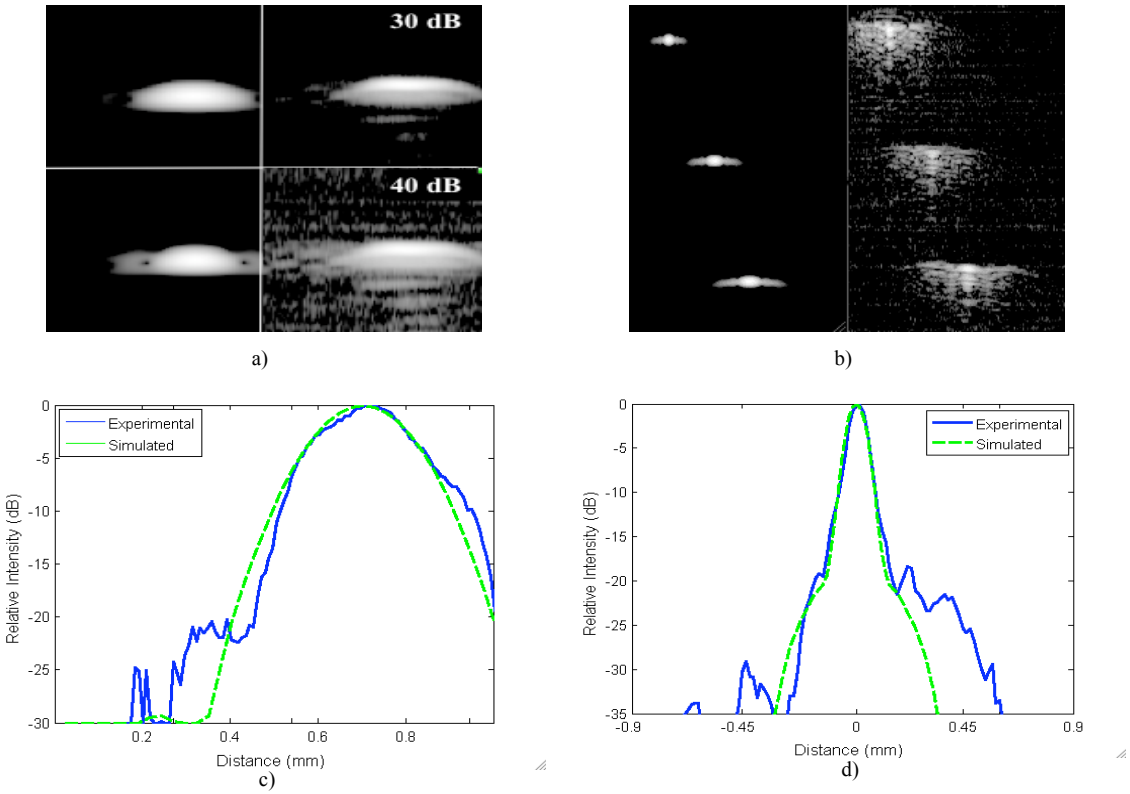

Figure 4.11. a) Experimental and simulated PSF for the target at f/2.7, frequency is 20 MHz. b) 50 MHz Experimental and simulated PSFs for f/1.9, f/2.9, f/3.8 c) 1-D cross-section of ρ=f/2.7 d) 1-cross-section of the target at f/3.8

4.4 Evaluation

The existing IVUS probes are examined thorough numerical simulations and are compared with rotating phased annular array configuration. We reconstructed 2-D PSFs for *f*/1, *f*/2 and *f*/3 and demonstrated that single transducer structure and annular array have identical beamwidth at *f*/2 as expected while the beamwidth of annular array at *f*/3 is narrower. Simulation results are experimentally validated by fabricated 0.84 mm diameter 8-element annular array. Experiment results show that, the lateral resolution of annular array is 250 μm and 120 μm for 20 MHz and 50 MHz. respectively. The simulated lateral resolutions are in agreement with these results. Both simulated and experimental results show that 8 element annular array is promising when compared to the size and performance of the existing annular arrays. The resolution performances of the annular CMUT arrays are suitable for dynamically focused image formation as shown by reconstructed B-scan images. Future works about this subject will consist of custom front-end ICs to construct phased data acquisition for phased array processing.

Chapter 5
Solid State Arrays

In this chapter we will introduce new solid-state cylindrical array configurations based on non-uniform aperture sampling, enabling realization of low-cost integrated phased array beamformers, which is shown in Figure 5.1. The probe architecture and its different configurations will be mentioned in the following section. Next section performs the comprehensive comparison between existing and proposed probes through simulated PSFs. Afterwards; the beamformer architecture will be discussed.

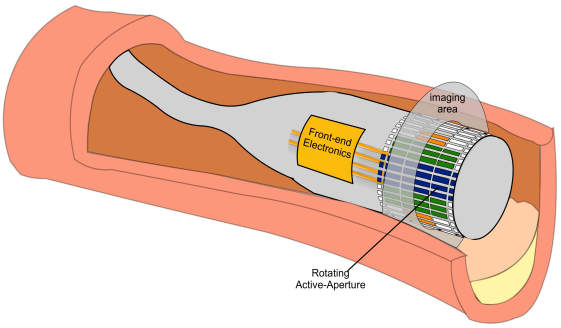

Figure 5.1 Illustration of solid-state with non-uniform sampled cylindrical array.

5.1 Probe Architecture

5.1.1 Non-Uniform Aperture Sampling

Uniform sampled cylindrical aperture shown in Figure 5.2 results in similar transducer impedance and sensitivity, however it provides comparatively high side-lobes at far field. In contrast, Non-uniform sampling suppresses the grating lobe and side-lobes, hence it causes lower side-lobe level at the cost of slightly wider main-lobe. Besides, wider central transducer worsens the near field imaging

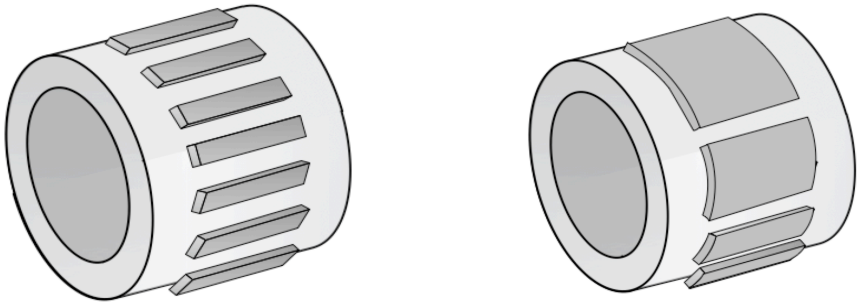

Figure 5.2 Uniform and non-uniform sampled cylindrical arrays.

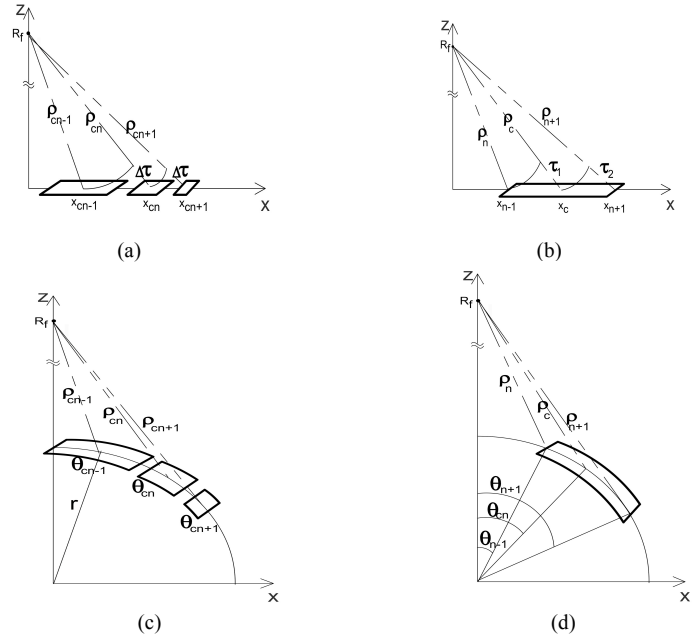

Figure 5.3 Geometrical setups to derive transducer locations and size; (a) and (b) illustrate planar array configuration; (c) and (d) show cylindrical array geometry.

performance [31]. We sample the transducer in order to obtain identical differential delays. This sampling scheme is referred as Fresnel sampling.

Element center locations are determined using the geometries shown in Figure 5.3(a) and Figure 5.3(c) in where, x_{cn} is the center of n^{th} transducer, ρ_n is the distance between transducer center and focal point R_f and the differential delay between adjacent transducer is $\Delta\tau$. The path difference should be equal in order to obtain identical differential delays. Calculation yields,

$$\Delta\rho = \rho_{n+1} - \rho_n = \frac{x_{cn+1}^2}{2R_f} - \frac{x_{cn}^2}{2R_f} \tag{5.1}$$

Identical differential delay and element locations are calculated by equating the path differences and using boundary conditions obtained by the locations of the first transducer and the last transducer. These boundary conditions are x_0=0 and x_N=D/2 for an N element array whose length is D. Obtained expressions are,

$$\Delta\tau = \frac{D^2}{8cR_fN}, \tag{5.2}$$

$$x_{cn}^2 = \frac{nD^2}{4N} \tag{5.3}$$

The velocity of ultrasound is represented by c in Equation 5.2. Calculated element locations represent their center; however the center means the delay differences to both edges are the same. Therefore $\Delta\tau_1$ and $\Delta\tau_2$ in Figure 5.3(b) should be equal. Using the center definition, transducer edges are determined as follows,

$$\Delta\tau_1 = \Delta\tau_2 \Rightarrow x_{cn} = \sqrt{0.5(x_n^2 + x_{n+1}^2)} \tag{5.4}$$

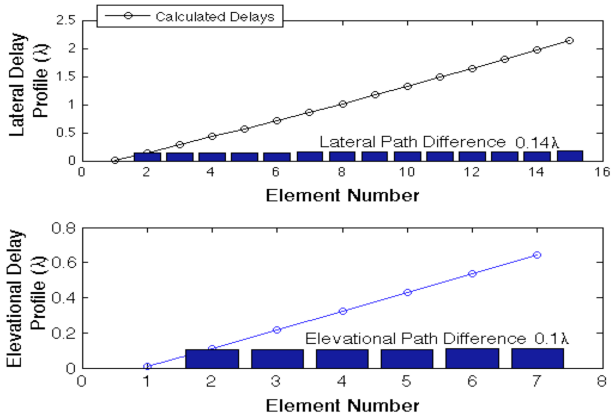

Figure 5.4 Calculated delay profiles and identical delay differences are illustrated, (a) 30 lateral elements (b) 14 elevational elements.

The Fresnel sampling for planar arrays was studied before [32,33]. Differently, we also sampled the cylindrical array employing the same principle. Used geometry is

illustrated in Figure 5.3(c) and Figure 5.3(d). Here, r is the radius of the cylindrical array, θ represents angular locations and the N-element array located between the angles θ_0 and θ_N. The path difference for cylindrical case is,

$$\Delta\rho = \rho_{n+1} - \rho_n = r\cos\theta_{cn} - r\cos\theta_{cn+1} \tag{5.5}$$

Using identical path difference condition and the location boundaries $\theta_0 = 0$ and θ_N, the identical differential delays and transducer locations are calculated,

$$\Delta\tau = \frac{r}{cN}(1-\cos\theta_N) \tag{5.6}$$

$$\cos\theta_{cn} = 1 - \frac{n}{N}(1-\cos\theta_N) \tag{5.7}$$

The angular width of each element satisfying the equal differential delays between center and edges condition, is given by the Equation 5.8

$$\cos\theta_{cn} = 0.5(\cos\theta_n + \cos\theta_{n+1}) \tag{5.8}$$

Therefore the Fresnel sampling can be employed not only for planar transducers but also in cylindrical case in order to use its benefits in both dimension of cylindrical aperture.

5.1.2 1-D Fresnel Sampled Active-Aperture Structure

Current solid-state transducer technology employs uniform element sampling providing the equal-area transducers, which maximize axial pressure. However it results a sinusoidal delay profile due to non-planar geometry. The differential delays of uniform sampled cylindrical array is,

$$\Delta\tau = \frac{r}{c}\sin(\frac{\theta}{2})\sin(\frac{(2n+1)\theta}{2}) \tag{5.9}$$

Where N is the number of transducers, r is the radius of cylindrical array whose angular width is θ. Equation 5.9 shows the differential delay depends on element number n, however they should be kept constant in order to simplify beam former.

We applied Fresnel sampling to the active-aperture of existing cylindrical array in order to equalize differential delays. The delay profile and differential delays for Fresnel sampled 30-element circular array are illustrated in Figure 5.4(a).

The circular array is oversampled to achieve Fresnel sampling precisely. Active-aperture elements are reformed in each rotational step and they are electrically connected to each other in order to satisfy the required element size. The same gray levels illustrate the same element in Figure 5.5(a) Identical differential delays enable integrated full phased array beam former, which improves SNR by √N whereas the image resolution is close to uniform sampled structure.

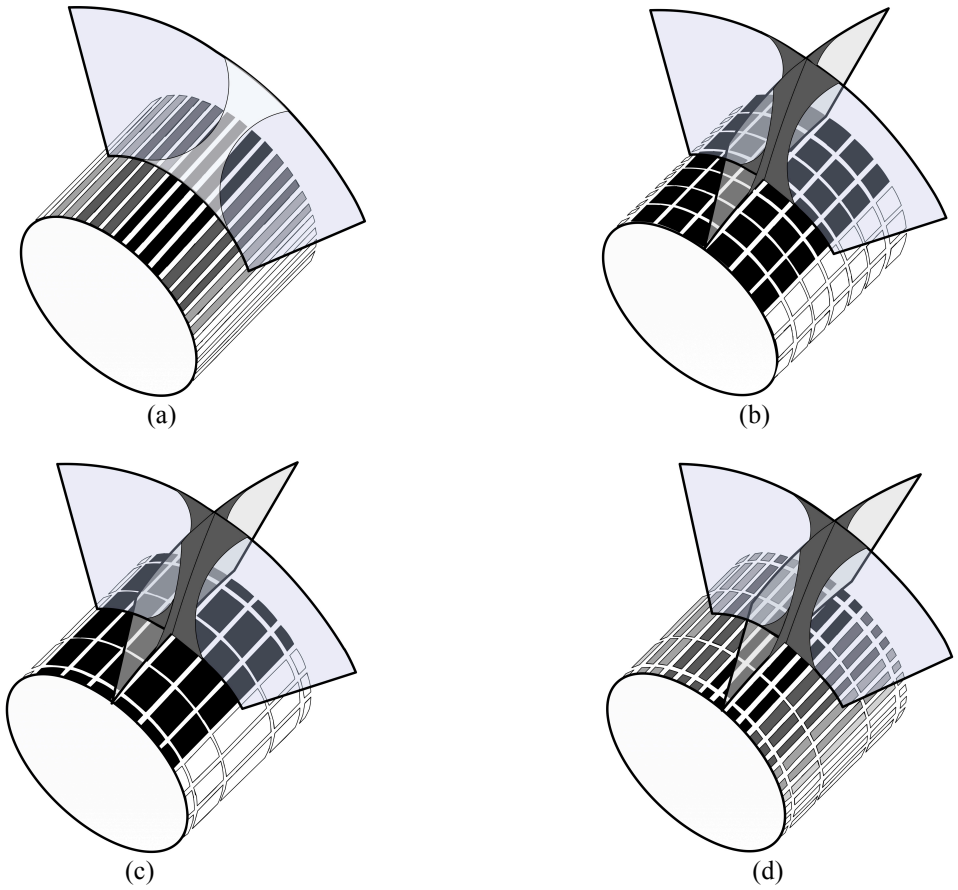

Figure 5.5 Investigated solid-state structures, rotating active-apertures are indicated by black and gray tones; (a) Fresnel Sampled 1D rotating rectangular active aperture (RAA-1D-FS) (b) Uniform sampled 2-D active-aperture (RAA-2D-US), (c) Elevationally Fresnel sampled 2D active-aperture (RAA-2D-EFS), (c) 2D active-aperture Fresnel sampled in both dimensions (RAA-2D-FS).

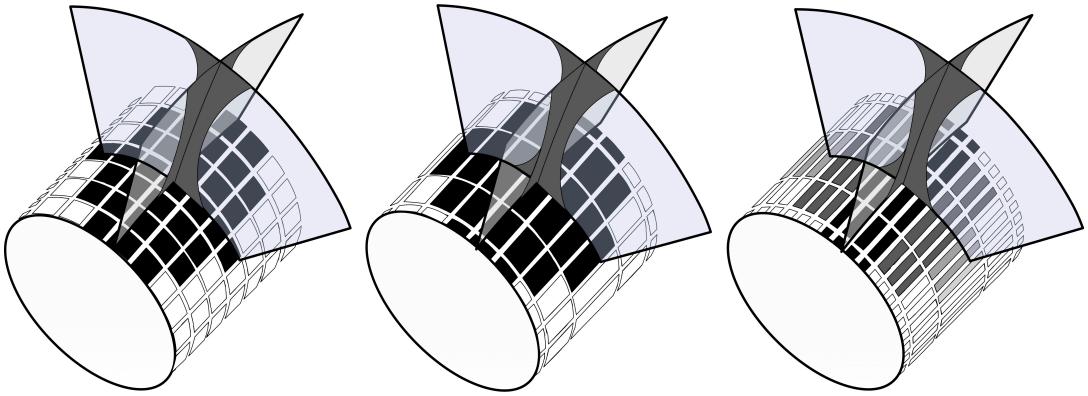

Figure 5.6 Disk Active-aperture Figures, Lateral and elevational B-scan cross-sections and generated beams are illustrated, (a) Uniform sampled 2D Disk active aperture (DAA-2D-US), (b) Elevational Fresnel sampled Disk Active aperture (DAA-2D-EFS), (c) Both dimension Fresnel sampled Disk Active-aperture (DAA-2D-FS)

5.2 2-Dimensional Active-Aperture Structures

Although presented 1D probes have great axial and lateral resolutions their elevation imaging performances are limited. Therefore the array is extended in that dimension to produce elevational beam for the sake of increased system complexity. The elevational array provides a rotating 2-D active aperture, which we applied varied sampling schemes. Although we constructed a 2D aperture, steering is not possible since the symmetry around central axis is employed. Therefore only central beam-line is constructed in each rotational step and this is enables separable elevational and lateral delays. Besides the symmetry halves the number of channels in both dimensions since the transducers with the same delay values are shorted. Elevational channels are shorted in fabrication but laterally; the connections must be reconfigured in each rotational step. The reconfiguration requires additional electronics that increases the complexity.

We simulated two different active aperture geometries: Rectangular Active Aperture (RAA) and Disk active aperture (DAA). Both geometries has several sapling schemes: 1) RAA, both dimension uniform sampled (RAA-2D-US): The cylindrical active-aperture is uniform sampled in both dimension as illustrated in Figure 5.5(b). The figure also shows its beam cross-sections. Although the structure is not practical due to unequal differential delays of uniform sampled array elements we investigate

RAA-2D-US as gold standard for comparison. 2) RAA, elevation dimension Fresnel sampled and uniform sampled laterally (RAA-2D-EFS): The structure illustrated in Figure 5.5(c) has identical differential delays only in elevation; therefore its lateral beamformer structure is still complex. However, RAA-2D-EFS simplifies elevation beamformer. The required electronics is reduced compared to RAA-2D-US but that reduction may not be enough for implementation of the probe.

Since the array is planar in elevation, the location and size of transducers are determined according to corresponding Fresnel sampling scheme described before. The delay profile and differential delays for 14 element planar array are presented in Figure 5.4(b).

3) RAA, both dimension Fresnel sampled (RAA-2D-FS): Since Fresnel sampling is applied in elevation and lateral dimensions the structure the beamformer complexity degraded in both dimension. Hence RAA-2D-FS structure is simple enough to implement a 2-D beam former constructing only the central beam-line in each rotational step. Figure 5.5(d) shows the illustration of RAA-2D-FS and its beam.

So far, we have described rectangular active-apertures. However, 2-D aperture enables several transducer geometries since each element in the non-steerable active aperture can be controlled separately. We demonstrated disk active aperture geometries since disk geometry improves resolution due to obtained axially symmetric beam. The annular array is much analyzed before since its capability of dynamic focusing and improved beam quality. However the mechanical rotation requirement is major drawback due to fabrication difficulties and axial movement originated image distortion. Alternatively solid-state rotating disk active aperture structure has defined fabrication process without mechanical rotation.

The probe architecture and beam former of rectangular active aperture-2D case remain unchanged. In contrast, only the transducers defining a disk aperture are activated. Figure 5.6(a) shows uniform sampled disk active aperture structure, which is unrealizable (DAA-2D-US). It has simulated for comparison. We also tested laterally uniform and elevational Fresnel sampled disk active-aperture structure (DAA-2D-EFS) illustrated in Figure 5.6(b). The structure enables a simple phased

array beam former implementation in elevation whereas laterally beamformer structure is complex.

Disk Active-aperture, which employs 2-D beam former, is illustrated in Figure 5.6(c). Fresnel sampled elevational and lateral aperture eliminates synthetic aperture imaging requirement. Hence DAA-2D-FS operates similar to AA in terms of imaging technique.

5.3 Performance Analysis

We tested the imaging performance using two-way PSF, the pulsed simulation method is expressed in section 4 is used. Here, receive mode f-number apodization is applied for the ranges smaller than *f*/2.

Table 5.1 Simulation Parameters

Exitation Pulse	Center Frequency: 20 MHz, FBW: 65% Sampling Frequency: 1GHZ
Ultrasound Velocity	1480 m/s
Catheter Diameter	840 µm
Target Distances	*f*/1, *f*/2, *f*/3

Table 5.2 Array Parameters

SL-IVUS Structure	Active Aperture Size (µm)	Number of Transducers	Element Pitch (µm)	Focusing Scheme
ST	Radius: 600	1	-	Fixed
RAA-1D-US	600×600	16×1	41	Dynamic × No focus
AA	Radius: 600	8	Variable	Dynamic
RAA-1D-FS	600×600	30×1	Variable	Dynamic × No focus
RAA-2D-US	600×600	16×14	41×43	Dynamic
RAA-2D-EFS	600×600	16×14	41×Var.	Dynamic
RAA-2D-FS	600×600	30×14	Var.×Var.	Dynamic
DAA-2D-US	Radius: 600	<16×14	41×43	Dynamic
DAA-2D-EFS	Radius: 600	<16×14	41×Var.	Dynamic
DAA-2D-FS	Radius: 600	<30×14	Var.×Var.	Dynamic

Figure 4.7 shows the array and the reference geometry used in simulations. The simulation parameters of different array types are chosen to enable fair comparison. Table 5.1 and Table 5.2 summarize these parameters. We used a 20 MHz Gaussian

pulse with 65% bandwidth. Numerical computer simulations are performed using three on axis point targets at ranges *f*/1,*f*/2 and *f*/3. Dynamic focusing schemes seen in Table II are only employed for receive modes since 2-way dynamic focusing is not practical, therefore the transmit focus of such probes is fixed focused to the depth *f*/2. Single transducer's transmit and receive focus is set to *f*/2 due to its mechanical focus. Cylindrical 1-D array structures have no focus in elevation while 2-D cylindrical structures are capable of dynamic focusing in that dimension.

5.3.1 Parameter Selection

We used 840-µm-catheter since the IVUS applications require small-sized catheters in the order of 1mm. Circumferential 64 array elements wrapped around the catheter is simulated for existing solid-state structure. The size of each transducer element is 42×600 µm. We sample the elements by 42-µm. pitches in both elevation and lateral dimensions. Element pitch of approximately 0.5λ at 20 MHz operating frequency is satisfactory because its grating lobe level is ignorable. Each rotational step activates 16-element sub-aperture, resulting in 600-µm active aperture size.

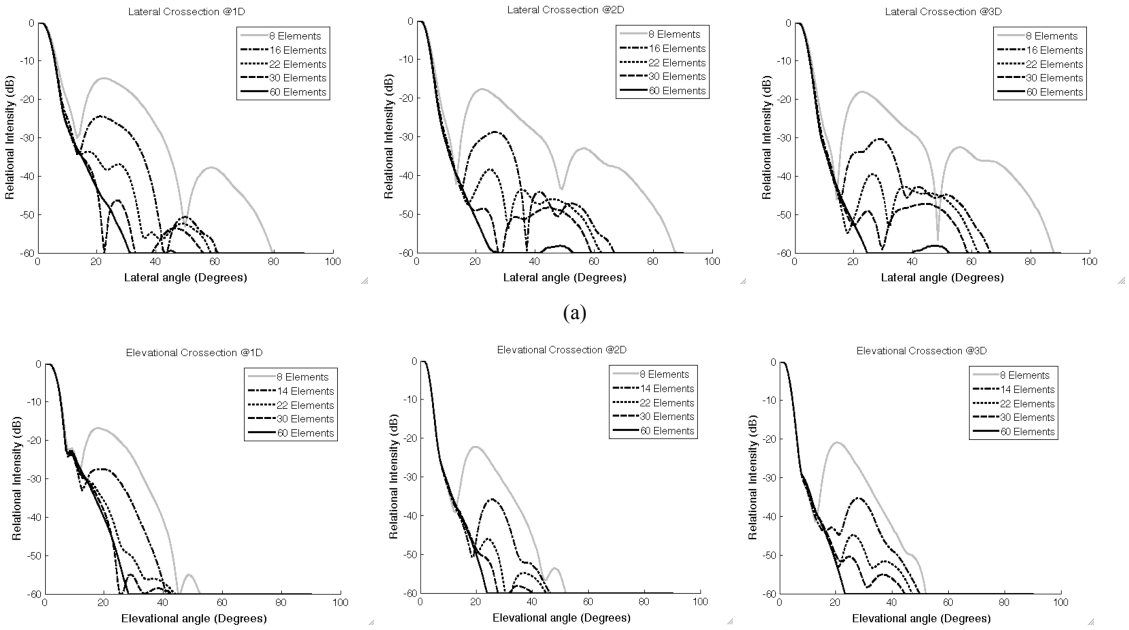

Figure 5.7 (a) Lateral and (b) Elevational Cross-sectional images of simulated PSF for non-uniform sampled 8 to 60 element cylindrical arrays at ranges *f*/1, *f*/2 and *f*/3.

The diameter of simulated 8-equal area concentric annular array is chosen the same as active aperture of solid-state in axial × azimuth dimensions. Rotating single transducer is also 600 μm in diameter and the same sampling was possessed as annular array case.

The number of activated lateral elements is the same in uniform and non-uniform sampled aperture solid-state structures. However the element number of non-uniform sampled active aperture should be increased in order to reduce sidelobe level, which should be under -40 dB laterally since it is enough for IVUS applications. Elevation sidelobes don't effects resolution directly therefore -30 dB sidelobe level is acceptable for elevation in order to reduce the complexity. The number of elements providing required sidelobe performance are determined using PSF simulations of non-uniform sampled lateral and elevational arrays with 8, 16, 22, 30, 60 and 8, 14, 22, 30, 60 elements respectively. The results are illustrated in Figure 5.7.

Even though the simulations show 22-element lateral and elevational arrays result sidelobes under 40 dB at all ranges we used 30-element lateral active aperture and 14-element array in elevation. So that lateral resolution is improved while elevation array satisfies -30 dB sidelobe level.

Another important parameter is the lateral pitch of oversampled cylindrical array since increased sampling reduces the quantization error; nevertheless, transducer technology limits element size, especially fabrication process of PZT results in finite kerfs between adjacent elements. Although CMUT transducer enables integration of small sized elements with small inter-element gaps, larger elements are preferable because of improved bandwidth and SNR. We have analyzed the quantization error in order to set the number of circumferential samples. Figure 5.8 illustrates lateral quantization errors, in where 16 elements active-aperture are formed using one fourth of 360,180 and 90 circumferential transducers. The maximum delay errors for 360,180 and 90 transducers are $\lambda/50$, $\lambda/7$ and $\lambda/8$ respectively. The delay error smaller than $\lambda/10$ is acceptable therefore 360 transducer elements were used in cylindrical array.

The diameter of disk formed in DAA structures was chosen as 600 μm in order to equalize active aperture size. The transducer group, which defines a 600-μm-diameter disk in active aperture, is activated in each rotational step.

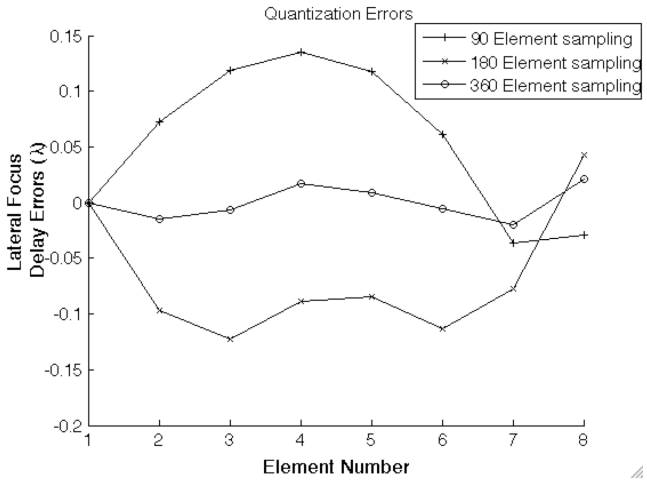

Figure 5.8 Non-uniform sampled 16 element Quantization errors for 360, 180 and 90 cylindrical array samples.

5.3.2 Simulation Results

We present the results using three individual sets for easy comparison. Each set consists of the beam cross-sections for elevational and lateral ρ-θ surfaces and φ-θ surface at three different ranges with 50 dB dynamic display range. Both elevational and lateral dimension of ρ-θ cross-sections are between -90, +90 degrees. Each ρ-θ window is 1200 μm in range direction. $\varphi\theta$-Surface is scanned by changing φ and θ between -180, +180 and 0, 90 degrees respectively. Figure 4.7 presents these cross-sections and simulation geometry.

The PSF simulations for existing structures are presented in chapter 4. We used the same simulations for comparison in this chapter again; Figure 5.9 illustrates that simulations. Simulations for proposed rectangular active aperture and disk active aperture probes are presented in Figure 5.10 and Figure 5.11, respectively. The 1-D cross-sectional images are obtained by averaging φ-θ cross-sections over θ for φ=0 (Lateral) and φ=90(Elevation) individually. Beamlines, whose θ angle is smaller than 6 dB-beamwidth, are used for averaging. These 1-D cross-sections are illustrated in

Figure 5.12, Figure 5.13 and Figure 5.14 for mentioned sets, in the same order. Table 5.3 and Table 5.4 summarize the parameters defining beam quality. We measured 6 dB and 20 dB beamwidths to refine point resolution and the sidelobe levels are presented to detect lateral resolution performance.

Table 5.3 Quantitative comparisons of lateral beams

SL-IVUS Structure	6-dB Beamwidth			20-dB Beamwidth			Far Sidelobe (F) Grating lobe (G) Level (dB)/Angle (Degrees)		
	1D	2D	3D	1D	2D	3D	1D	2D	3D
ST	10.78	6.01	6.85	17.38	11.12	12.2	-	-	-
RAA-1D-US	7.92	6.85	7.07	16.46	13.67	12.92	52/55(G)	-58/62(G)	-
AA	9.74	6.01	6.66	17.58	11.12	12.3	-	-	-
RAA-1D-FS	7.97	6.9	7.17	16.65	13.91	13.08	-	-	-
RAA-2D-US	7.72	6.33	6.69	13.95	11.72	12.29	-56/56	-57/65(G)	-58/67(G)
RAA-2D-EFS	7.76	6.35	6.7	14.16	11.76	12.31	-58/58	-57/65(G)	-59/67(G)
RAA-2D-FS	7.83	6.88	6.91	14.39	12.28	12.59	-	-59/43(F)	-58/41(F)
DAA-2D-US	8.9	6.97	7.2	16.78	13.03	13.49	-60/51	-60/62(G)	-
DAA-2D-EFS	9.42	7	7.21	17.82	13.11	13.53	-	-59/64(G)	-
DAA-2D-FS	9.28	7.04	7.31	17.56	13.33	13.8	-	-	-

Table 5.4 Quantitative comparisons of Elevation beams

SL-IVUS Structure	6-dB Beamwidth			20-dB Beamwidth			Sidelobe Level (dB)/Angle (Degrees)		
	1D	2D	3D	1D	2D	3D	1D	2D	3D
ST	10.78	6.01	6.85	17.39	11.12	12.2	-	-	-
RAA-1D-US	26.09	14.01	8.68	33.1	23.49	15.4	-33/29	-34/18	-40/21
AA	9.74	6.01	6.66	17.58	11.12	12.3	-	-	-
RAA-1D-FS	26.22	13.83	8.69	33.18	23.48	15.3	-33/29	-34/18	-40/21
RAA-2D-US	7.78	5.5	5.97	12.52	10.1	10.78	-	-	-
RAA-2D-EFS	7.72	5.6	6.03	12.51	10.19	10.92	-32/16	-44/25	-44/27
RAA-2D-FS	7.73	5.89	6.22	12.57	10.61	11.09	-32/16	-43/25	-44/27
DAA-2D-US	10.19	5.94	6.36	18.28	10.98	11.73	-	-	-
DAA-2D-EFS	9.38	6.2	6.58	16.73	11.51	12.28	-31/23	-44/22	-44/21
DAA-2D-FS	9.65	6.12	6.56	17.38	11.41	12.22	-32/23	-45/23	-45/21

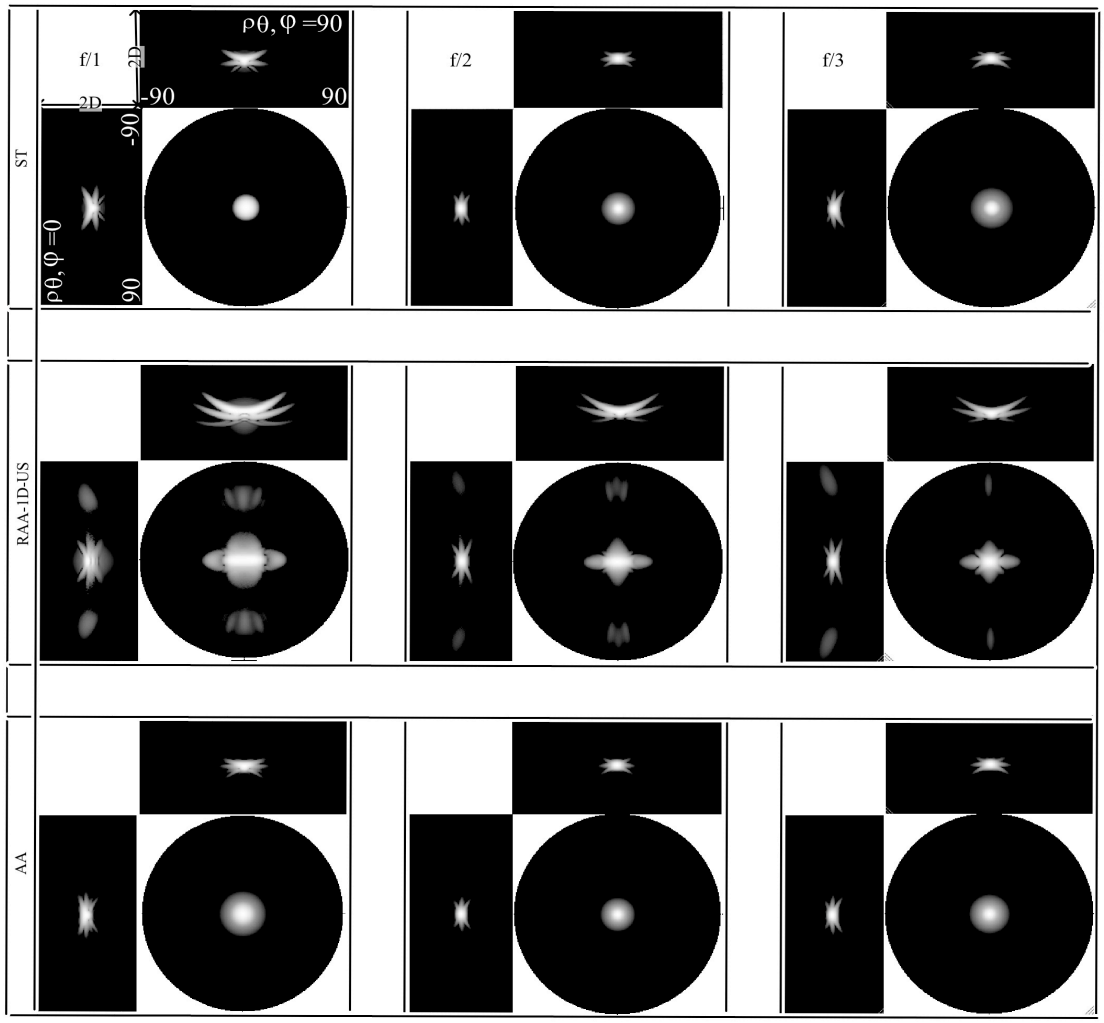

Figure 5.9 Beam patterns of existing probe types are illustrated with a dynamic display range of 50 dB. Constant ρ, elevational and lateral cross-sections for ST, RAA-1D-US and AA structures are presented at ranges *f*/1, *f*/2 and *f*/3.

As mentioned in chapter 4, Figure 5.9 shows the ST structure is poor in lateral resolution at the out of focal region; both ST and AA have axysimmetric beams due to their geometry. Although RAA-1D-US also enables dynamic focusing the beam at focal range *f*/2 is slightly wider due to 1D-cylindrical array geometry. In other words element directivities cause the increased beamwidth. However that wideness is not significant. Simulated PSFs show, the leading disadvantages of RAA-1D-US are the lack of poor elevation beam and low SNR limited by synthetic aperture imaging.

We proposed RAA-1D-FS structure to solve the poor SNR problem. RAA-1D-FS employs full-phased lateral array, which improves the SNR by the factor of $\sqrt{N_L}$, where N_L is the element number in active aperture. Its simulation results presented in Figure 5.9 that shows RAA-1D-FS and RAA-1D-US have similar performances. Their 6 dB beamwidths are almost the same at all ranges. There is no noticeable

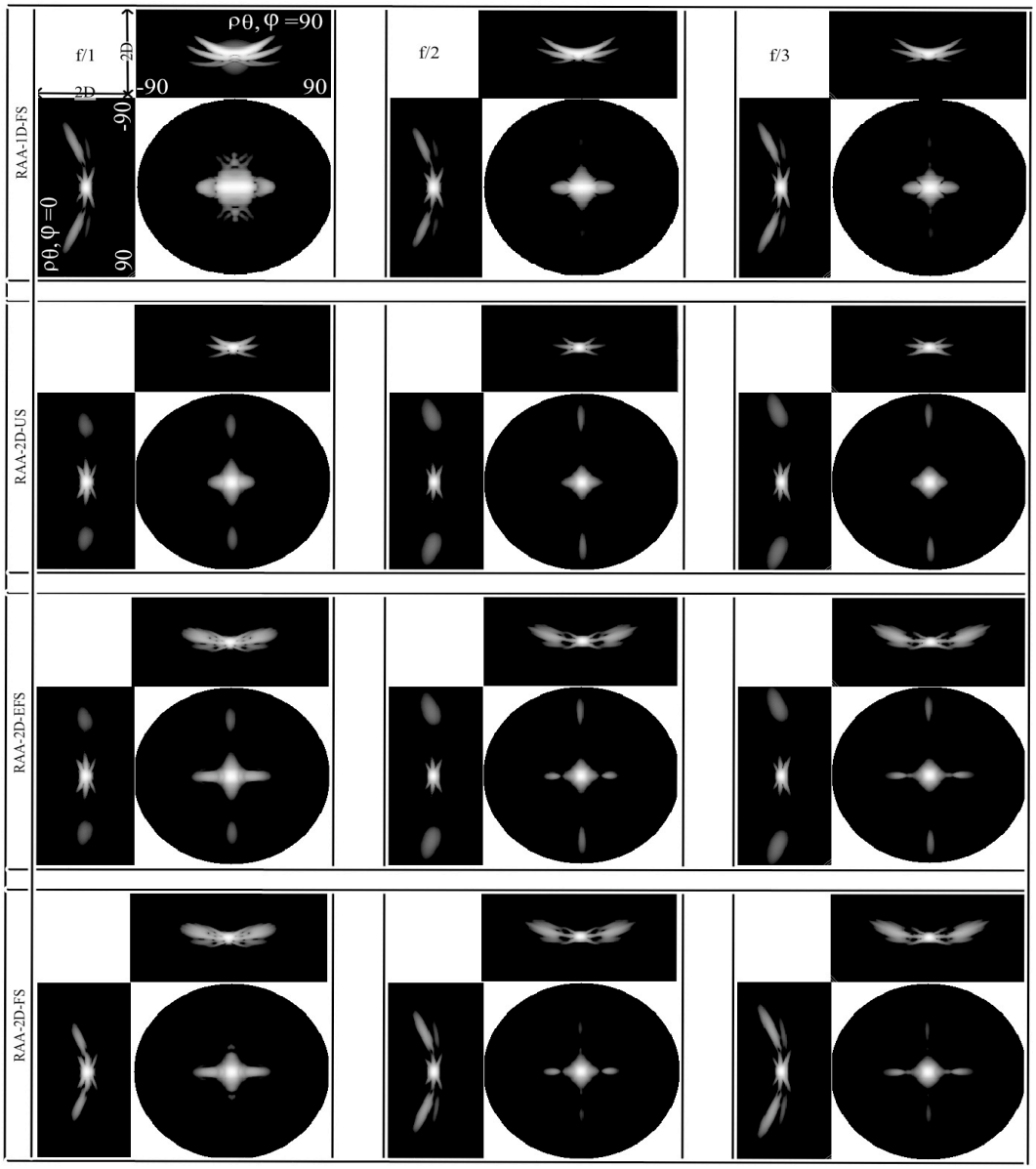

Figure 5.10 PSF simulation results for rectangular active aperture structures; the dynamic display range is 50 dB. The cross-sectional B-scan and C-scan images are presented for RAA-1D-FS, RAA-2D-US, RAA-2D-EFS and RAA-2D-FS structures.

widening of beam at 20 dB, the difference of 20 dB beamwidths are about 0.2°. RAA-1D-FS has the same elevation characteristic due to absence of elevation array extension.

We explored RAA-2D structures to overcome the lock of elevation focusing. The uniform sampled RAA-2D-US array is not realizable. It is simulated to demonstrate the best beam performance provided by that size array. The simulation results for

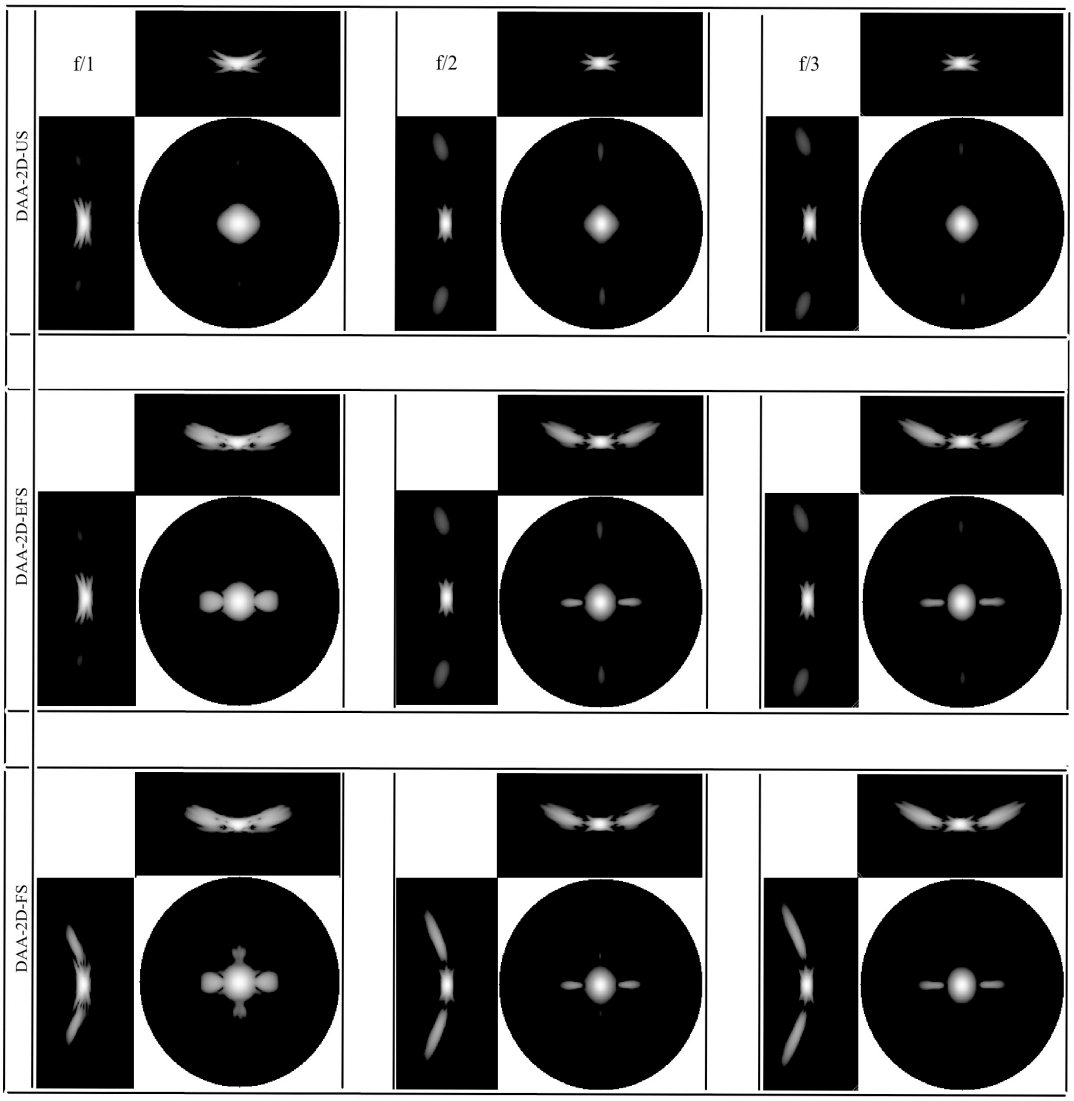

Figure 5.11 The cross-sectional images of beam patterns of disk active aperture structures at ranges, *f*/1, *f*/2 and *f*/3. Images are presented with dynamic display range of 50 dB.

RAA-2D structures are illustrated in Figure 5.10 and corresponding 1-D plots are in Figure 5.13. RAA-2D-EFS and RAA-2D-FS structures provide remarkable improvement in beam quality over 1-D solid-state structure; the beams are almost the same as uniformly sampled, full-phased 2-D array. The lateral beams of RAA-2D-US and RAA-2D-EFS are the same since for both of them have uniformly sampled array in that dimension. RAA-2D-FS has slightly widened beam at all ranges; the maximum widening is 0.4°. In elevation, the improvement over RAA-1D structures is remarkable; 6 dB beamwidths are reduced by 18°, 8.5° and 2.7° at ranges *f*/1,

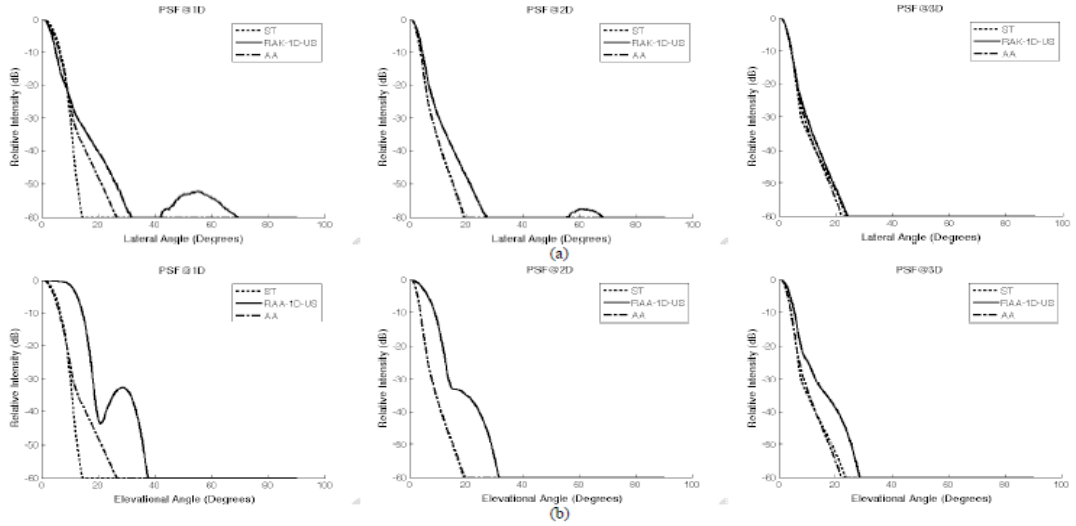

Figure 5.12 (a)Lateral, (b)Elevational Cross-sectional beam patterns for existing probe types.

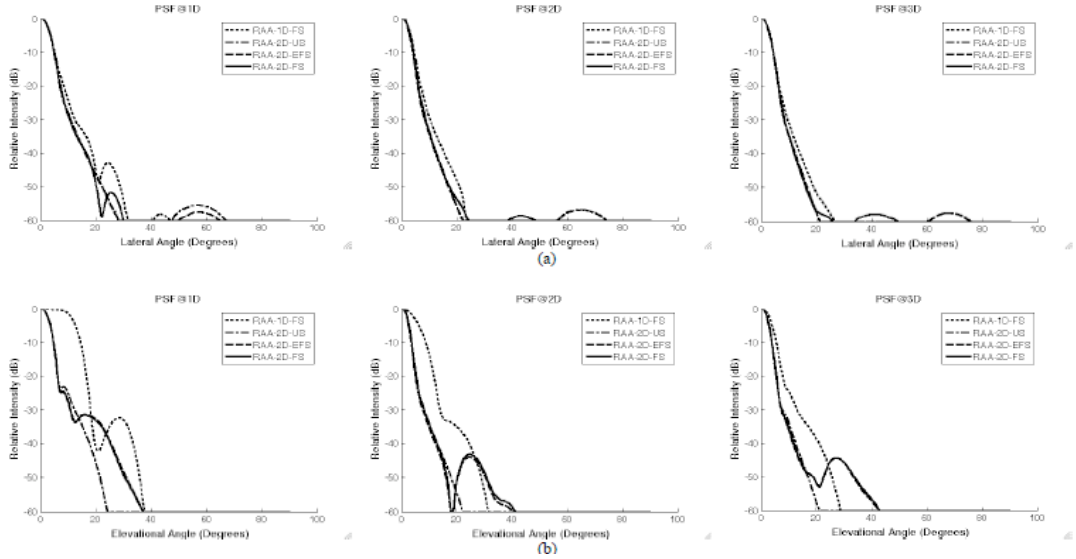

Figure 5.13 (a)Lateral, (b)Elevational Cross-sectional beam patterns for RAA structures.

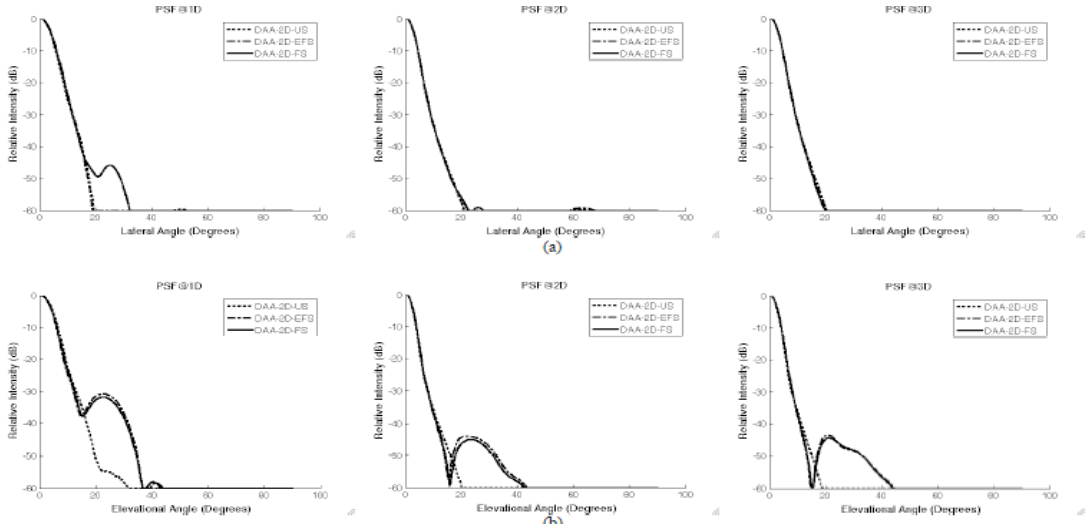

Figure 5.14 (a)Lateral, (b)Elevational Cross-sectional beam patterns for DAA structures.

f/2 and *f*/3 respectively. The elevation beamwidth differences between RAA-2D structures are not noticeable. Side-lobes of non-uniform sampled structures are under 40 dB and 30 dB for lateral and elevation dimension respectively.

The PSF simulation results of disk active aperture are summarized in Figure 5.11 and Figure 5.14. DAA-2D-US is the hypothetical case simulated for comparison. The non-uniform sampling does not result a considerable widening in PSF compared to DAA-2D-US case. Disk aperture provides almost circular symmetric main lobe with side-lobe levels less than 40 dB. Elevational and lateral 6-dB beamwidths of DAA cases are close. The 6 dB and 20 dB beamwidths of AA structure and DAA-2D structures are almost the same; the maximum difference is 0.2° in elevation and 1° in lateral dimension.

The simulation results show that 2-D structures provide remarkable resolution improvement if they compared to existing solid-state structure. RAA-1D-FS and existing solid-state structure have similar beams whereas RAA-1D-FS improves SNR by enabling phased array. Disk Active aperture structures also improve the resolution compared to solid-state 1-D array. In addition they perform almost the same beam performance as AA structure, in contrast DAA structures can electronically rotatable. The overall simulation results of non-uniform sampled arrays demonstrate promising performance in terms of their beam qualities.

5.3.3 Beamformer Architecture

The main necessity of non-uniform sampled aperture is a realizable beam former design. The Rectangular 2-D aperture cannot be integrated to an IVUS probe since the complex beam former architecture of excessive number of transducers. Annular array is an alternative design reducing the beam former size, however it requires mechanical scanning. The circumferential 2D array is only way of designing electronically rotating, high-resolution IVUS probe; therefore beam former structure must be simplified.

One can design a 1-D beam former for a uniform sampled aperture as illustrated in Figure 5.15(a) in which the delays are applied each channel individually. The

difference delay elements are employed since non-linear delay profile of uniform sampled array. However realization of different delay elements for excessive number of channels is difficult for IVUS applications. Figure 5.15(c) presents a beam former, which employs identical delay elements, for uniform sampled planar arrays. In that case required number of delay elements is proportional to square of the number of transducers resulting dramatically increase of beam former size. The Figure 5.15(b) and Figure 5.15(c) illustrate the beam formers according to delay profile of planar array, For cylindrical apertures delay profile is sinusoidal resulting differential delay proportional to a sinusoidal function; the beamformer structure in Figure 5.15(a) is proper for a cylindrical aperture. Similarly, delay differences also has dependency of element number, hence beam former of uniform sampled cylindrical structures are also not realizable, that is why we used Fresnel sampling to obtain identical delay differences which decreases the order of the required number of delay elements from N^2 to N. The Illustration of beam former for 1D, Fresnel sampled 1-D planar array is presented in Figure 5.15(c). The beamformer size is proportional to, *N/2*. Total number of element N is halved due to employed symmetry.

Fresnel sampling in both dimension transforms the complex 2-D beam former into a separable beam former that requires simple 1-D beam formers. That structure is illustrated in Figure 5.15(d), where $1\times N_E/2$ beamformer should be used to form elevational beam. The constant delay value for elevation array is analyzed and given by Equation 5.2. Laterally beam formed signals summed using a $1\times N_L/2$ lateral beam former, corresponding differential delay is given by Equation 5.6. Therefore we need $1\times N_L/2$ pieces of lateral beam formers. In other words, $(N_L/2)\times(N_E/2)$ beamformer operates full-phased 2-D array. Comparatively a uniform sampled 2-D. transducer array requires the beamformer size of, $\frac{N_L(N_L-2)}{8}\times\frac{N_E(N_E-2)}{8}$.

For instance, uniform sampled 16×14-element planar array requires 28 pieces of 14×1 beam former; whereas 16×14-element Fresnel sampled structure needs 8 pieces of 7×1 beam former. The size of beam former decreased dramatically. Since the dependency on number of element decreased dramatically, the number transducer can be increased to improve depth of field. We used 30×14 Fresnel sampled array in

order to increase the beam quality. The beam former complexity for that size is 15×7, which is much simpler than beam former for uniform sampled aperture.The proposed beam former structure can be integrated to a small sized IVUS catheter and enables 2D phased array, which improves image SNR significantly.

5.4 Evaluation

We evaluated the existing SL-IVUS probes and proposed a new solid-state structure enabling different electronically rotating geometries together with the advantage of phased array beam forming. The laterally Fresnel sampled 1-D structure eliminates the need of synthetic aperture beam forming thus improves SNR by the factor of $\sqrt{N}$, whereas the beam quality of two case is similar. However, the elevation resolutions of 1-D structures are very poor. We investigated 2-D cylindrical array configurations by adding the elevation extension. The uniform and non-uniform sampled rectangular and disk shape rotating apertures are explored and their performances are promising to implement an IVUS probe, which has electronically rotating 2-D aperture with different geometries. Detailed performance comparison is completed through excessive number of PSF simulations. Annular array and electronically rotatable disk performs similar beams, whereas rotatable disk has no mechanical part. Wider center element of Fresnel sampled structures results slightly increase of beam-width as expected. The difference is made ignorable by increasing the number of transducers in Fresnel sampled array.

Additionally proper beam former structures are investigated for each solid-state design, in terms of beam former complexity. The realization of these probes is discussed. The beam former structures for Fresnel sampled aperture needs less resources; hence they may lead up phased array beam forming for solid-state arrays. Besides, the structures, which have phased array in elevation and synthetic aperture beam forming in lateral, were discussed. They enable dynamic elevation and lateral focusing, where synthetic aperture imaging is employed.

The method enables successive integration of full phased 2-D array to a small sized IVUS probe. We plan to realize the design using CMUT elements integrated with analog beam former.

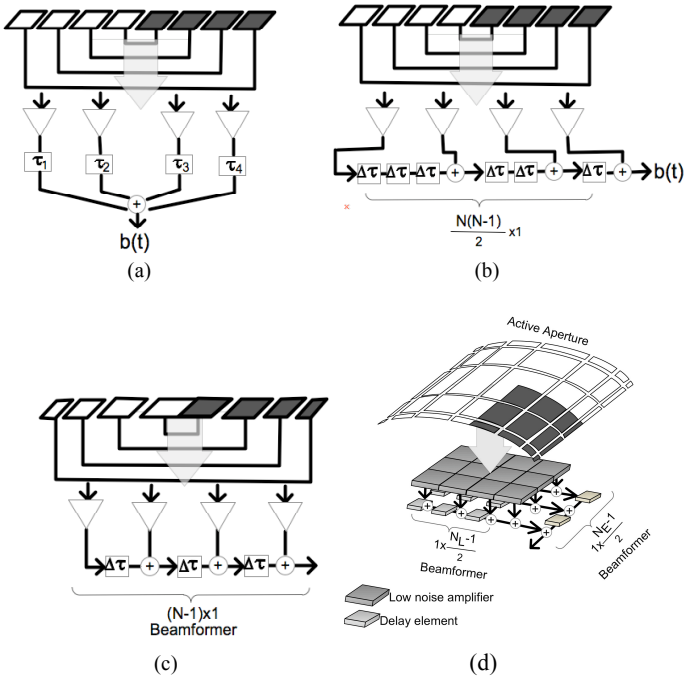

Figure 5.15 Uniform and non-uniform sampled beam former structures; axial symmetry of 2D array halves the channels in each dimension, (a) Uniform sampled array with different delay elements, (b) Uniform sampled array with identical delay elements, (c) Beam former illustration of Fresnel sampled array, (c) Illustration of beam former structure for solid-state 2-D Fresnel sampled aperture.

Chapter 6
Conclusion

In this dissertation, we focused on particularly IVUS technology, which leads many advances in the area of invasive vascular techniques. Although conventional angiography visualizes the plaque structures for diagnosis purposes and leads successful therapeutic operations like stent deployment or balloon dilation, this technology has reached its limits. The rapid advances in ultrasound technology after 1990s, make these applications practical. Furthermore IVUS promises new unique applications like visualizing the structure of plaque or vessel interior surface. Additionally the technology enables 3D imaging, which provides required cross-sectional images. IVUS probes can measure the differential pressure the both edges of a deployed stent and that is very useful to decide operation success. The latest advances also enable blood flow imaging. Further works are still in progress involving real-time 3D imaging, improving the image resolution, more compact electronics integration and high bandwidth, high performance, low profile transducers.

The currently used probes utilize either single transducer or circumferential array. Single transducer scanners have simple fabrication and great axial resolution; however, they suffer from motion artifacts and fixed focus operation results poor resolution. In contrast solid-state high-density array enables dynamic focusing with no mechanical rotation at the cost of reduced elevation performance and increased electronic complexity. We demonstrated that annular array performs better; the main lobe width is almost the same as single transducer at f/2. Therefore annular array is well approximated to precisely focused full disk aperture. Out of focal depth, at ranges f/1 and f/3, annular array has narrower beams as expected. The results for annular array are validated by experimental studies are presented in Chapter 4. The

results of 50 MHz annular-array are challenging and state the CMUT implementation of 840 μm-diameter array is possible with outstanding bandwidth and resolution.

Solid-state structure has a significant advantage over mechanical scanners due to it eliminates mechanical distortions. However the acceptance angle problem, poor SNR and wider elevation beam are the problems of solid-state structure. Acceptance angle is a physical constraint that has not significant effect on image quality. Hence we concentrated to solve the SNR problem and to improve image thickness. In Chapter 5 we introduce a new 2-D solid-state circumferential array structure enables the electronic rotation of any required geometry with improved SNR and elevation performance. Electronically rotating rectangular and disk structures are tested through computer simulations. The results show elevation performance is improved significantly compared to conventional solid-state structure. Simplified beamformer enables phased array imaging which improves SNR and decreases the motion susceptibility.

We used 20-MHz and 65% FBW pulse in simulation of solid state atructures. The uniform and Fresnel sampled 1-D ring arrays perform similarly in terms of beam quality while the latter approach improves image SNR by a factor of $\sqrt{N_L}$ due to synthetic versus full phased array processing. The Fresnel sampled 2-D array performs dramatically better in elevation compared to 1-D ring array; the measured 6-dB lateral/elevational beamwidths of PSFs at f/2 are approximately 7/7 and 7/14 degrees, respectively. The additional contribution of 2-D array on image quality is high SNR produced by phased array beamforming.

Trend shows, near future will raise impressive developments on IVUS technology. The recent advances in transducer technology and semiconductor technology enable further miniaturization. That encourages improved IVUS structure which will represent the gold standard.

References

[1] Hunt, F. V., *Origins of Acoustics. New Haven*, CT: Yale Univ, Press, 1978.

[2] Hunt, F. V., *Electroacoustics: The Analysis of Transduction, and Its Historical Background.* New York: Acoustical Society of America, 1982.

[3] Erikson, K. R., Fry, F. J., and Jones, J. P., "Ultrasound in Medicine—A Review", *IEEE Trans. Sonics Ultrason.* **SU-21,** 144–170 (1974).

[4] Mason, W. P., "Sonics and ultrasonics: Early History and Applications", *IEEE Trans. Sonics Ultrason.* **SU-23**, 224 –232 (1976).

[5] O'Brien, W. D., Jr., "Assessing the Risks for Modern Diagnostic Ultrasound Imaging", *Jpn. J. Appl. Phys.* **37**, 2781–2788 (1998).

[6] Steinberg, B. D., *Principles of Aperture and Array System Design.*, Wiley-Interscience Publication, 1976.

[7] Bjorn, A. J., *Waves, Signals, and Signal Processing.*, Emantec AS, 2000.

[8] Erguri, A.S., Yongli, H. X. Z., Oralkan, O., Yarahoglu, G.G., Khuri-Yakub, B.T., Capacitive micromachined ultrasonic transducers: fabrication technology*, IEEE Trans. Ultrason., Ferroelectric., Freq. Contr*. **52**(12), 2242-2258 (2005).

[9] Kai, E. T., *Evolution of Ultrasound Beamformers,* IEEE Trans. Ultrason., Ferroelectric., Freq. Contr. **2**, 1615-1622 (1996).

[10] Jensen, J.A., *Linear description of ultrasound imaging systems, Notes for the International Summer School on Advanced Ultrasound Imaging*, Technical University of Denmark, 1999.

[11] Karaman, M., Tavlı, B., *Efficient Ultrasonic Synthetic Aperture Imaging,* IEEE Electronic Letters **35**(16), 1319-1320 (1999).

[12] Karaman, M., Li, P. C., O'Donnell, M., *Synthetic Aperture Imaging for Small Scale Systems, IEEE Trans. Ultrason., Ferroelectric., Freq. Contr*. **42**(3), 429-442 (1995).

[13] Kaneda, H., Honda, Y., Yock, P. G., Fitzgerald P. J., *What do Cardiologists Want from Ultrasound? Vascular Ultrasound,* Springer-Verlag, Tokyo, 3-28.

[14] Knight, J., McLean, J., and Degertekin, F. L., "Low Temperature Fabrication of Immersion Capacitive Micromachined Ultrasonic Transducers on Silicon and Dielectric Substrates", *IEEE Trans. Ultrason., Ferroelectric., Freq. Contr.* **51**, 1324-1333 (2004).

[15] Choi, C. D., Skovoroda, A. R., Emelianov, S. Y. and O'Donnell, M., "Strain Imaging of Vascular Pathologies Using a Compliant Balloon Catheter". *IEEE Ultrasonics Sympozium* **2**, 1771-1774 (2000).

[16] Choi, C.D., Savage, J., Stephens, D.N., O'Donnell, M., "Stent Deployment Using an Integrated Semi-Compliant Balloon Ultrasound Catheter", *IEEE Ultrasonics Symposium* **2**, 1795-1798 (2002).

[17] Oralkan, O., Hansen, S. T., Bayram, B., Yaralioglu, G. G., Ergun, A. S., and Khuri-Yakub, B. T., "High-Frequency CMUT Arrays for High-Resolution Medical Imaging", *IEEE Ultrasonics Symposium* **1**, 399- 402 (2004).

[18] Fisher, R., Thomenius, K., Wodnicki, R., Thomas, R., Cogan, S., Hazard, C., Lee, W., Mills, D., Khuri-Yakub, B., Ergun, A., Yaralioglu, G., "Reconfigurable Arrays for Portable Ultrasound", *IEEE Ultrasonics Sympozium*, 495-499 (2005).

[19] Van den Steen, A. F. W. and Saijo, Y., *Vascular ultrasound,* Springer-Verlag, Tokyo, 2003.

[20] Kortbek, J., Arendt Jensen, J., Lokke Gammelmarkt, K., "Synthetic Aperture Focusing Applied to Imaging Using a Rotating Single Element Transducer", *IEEE Ultrasonics Symposium*, 1504-1507 (2007).

[21] Frazier, C.H., O'Brien, W.D. Jr., "Synthetic Aperture Imaging with a Virtual Source Element", *IEEE Ultrasonics Symposium* **2**, 1504-1507 (1996).

[22] Meng-Lin, L., Wei-Jung, G., Pai-Chi, L., "Synthetic Aperture Imaging with a Virtual Source Element", *IEEE Trans. Ultrason., Ferroelectric., Freq. Contr.* **51**, 63-70 (2004).

[23] Jerome, M. G., Borsboom, E., Ignacio, C., Van der Steen, A. F. W., Charles, T. L., Deprettere, E. F., "Simulation of Circular Array Ultrasound Transducers for Intravascular Applications", *J. Acoust. Soc. Am.* **2**, 827-835 (2000).

[24] O'Donnell, M., Thomas, L. J., "Efficient Synthetic Aperture Imaging from a Circular Aperture with Possible Application to Catheter-Based Imaging", *IEEE Trans. Ultrason., Ferroelectric., Freq. Contr.* **39**(3), 366-380 (1992).

[25] Shapo, B. M., O'Donnell, M., "Efficient Synthetic Aperture-Based Imaging from a Circular Array: Experimental results on a catheter probe", *IEEE Ultrasonics Sympozium* **44**, 1099-1102, (1993).

[26] O'Donnell, M, Eberle, M. J., Stephens, D. N., Litzza, J. L., Vicente, K. S., Shapo, B. M., "Synthetic Phased Arrays for Intraluminal Imaging of Coronary Arteries", *IEEE Trans. Ultrason., Ferroelectric., Freq. Contr.* **44**, 714-21 (1997).

[27] Hazard, C. R., Fisher, R. A., Mills, D. M., Smith, L. S., Thomenius, K. E., and Wodnicki, R. G., "Annular Array Beamforming for 2D Arrays with Reduced System Channels", *IEEE Ultrasonics Symposium*, 1853-1861 (2003).

[28] Brown, J. A., Démoré, C. E. M. and Lockwood, G. L., "Design and Fabrication of Annular Arrays for High-Frequency Ultrasound", *IEEE Trans. Ultrason., Ferroelectric., Freq. Contr.* **51**(8), 1010-1017 (2004).

[29] Sisman, A., Zahorian, J., Gurun, G., Karaman, M., Balantekin, M., Degertekin, F. L., Hasler, P., "Evaluation of CMUT Annular Arrays for Side Looking Intravascular Ultrasound Imaging", *IEEE Ultrasonics Symposium*, 84-87 (2009).

[30] Zahorian, J., Guldiken, R., Gurun, G., Qureshi, M. S., Balantekin, M., Degertekin, F. L., Carlier, S., Sisman, A., Karaman, M., "Annular CMUT Arrays for Side Looking Intravascular Ultrasound Imaging", *IEEE Ultrasonics Symposium*, 84-87 (2007).

[31] Daft, C. M. W., Wildes, D. G., Thomas, L. J., Smith, L. S., Lewandowski, R. S., Hue, W. M., Rigby, K. W., Chalek, C.L. and Hatfield, W. T., "A 1.5D Transducer for Medical Ultrasound", *IEEE Ultrasonics Symposium*, 1491-1495 (1997).

[32] Wildes, D. G., Chiao, R. Y., Darft, C. M. W., Rigby, K. W., Smith, L. S., Thomenius, K. E., "Elevation Performance of 1.25D and 1.5D Transducer Arrays", *IEEE Trans. Ultrason., Ferroelectric., Freq. Contr.* **44**(5), 1027-1037 (1997).

[33] Anderson, R. C., Desilets, C. S., Whelchel, L. E., "Development of A 1.5D, 1536 Element Ultrasonic Array for Use with Integrated Electronics", *IEEE Ultrasonics Symposium*, 1199-1202 (1999).

Appendix A PSF Derivations

PSF of an annulus transducer is derived here, the center coordinates of annulus is x=0,y=0,z=*z*. The radius of annulus is r. Point target is located to constant φ surface at point, P(r'sinθ, 0, r'cosθ).

The distance between a point in annulus (rcosφ, 0, rsinφ) and point P(r'sinθ, 0, r'cosθ) is,

$$\rho = \sqrt{(r'\cos\phi)^2 + (r\sin\theta - r'\sin\phi)^2 + (r\cos\theta - z')^2}$$

$$\rho = \sqrt{r'^2 - 2rr'\sin\theta\sin\phi + r^2 + z^2 - 2zr\cos\theta}$$

$$\rho = r\sqrt{\frac{r'^2}{r^2} + \frac{z'^2}{r^2} - \frac{2rr'\sin\theta\sin\phi}{r^2} - \frac{2rz'\cos\theta}{r^2} + 1}$$

Far field assumption, $r >> r', r >> z'$

$$\rightarrow \rho \approx r(-\frac{2rz'\cos\theta}{r^2} - \frac{2rr'\sin\theta\sin\phi}{r^2} + 1) = r - z'\cos\theta - r'\sin\theta\sin\phi$$

$$PSF(\theta) = \iint_{\phi,r'} r' e^{jk\rho}\, d\phi\, dr'$$

$$PSF(\theta,z) = e^{-jkz'\cos\theta}\int_a^b r'\, dr'(\int_{-\pi}^{\pi} e^{-jkr'\sin\theta\sin\phi}\, d\phi)$$

use the zeroth order Bessel function definition, $J_0(u) = \frac{1}{\pi}\int_0^{\pi} e^{ju\cos\theta} d\theta$;

$$PSF(\theta,z) == e^{-jkz'\cos\theta}\frac{2}{\pi}\int_a^b r' J_0(kr'\sin\theta)\, dr'$$

use the Bessel identity, $\int_0^u u' J_o(u')\, du' = uJ_1(u)$,

$$PSF(\theta,z) = e^{-jkz'\cos\theta}\frac{2}{\pi}\int_a^b r' J_0(kr'\sin\theta)\, dr' = \frac{2r'e^{-jkz'\cos\theta}}{\pi k\sin\theta} J_1(kr'\sin\theta)\Big|_{r'=a}^{b}$$

For z=0,

$$PSF(\theta,0)=\frac{2r'}{\pi k\sin\theta}J_1(kr'\sin\theta)\Big|_{r'=a}^{b}.$$

For the array of concentric annuli, we should sum their individual PSFs,

$$PSF_{AA}(\theta)=\sum_i\frac{r'}{k\sin\theta}J_1(kr'\sin\theta)\Big|_{r'=a_i}^{b_i},$$

Here a_i and b_i are the inner and outer radii of each annulus. The equation is given in chapter 4.

For circumferential array wrapped to the cylinder along π degrees, The radius of cylinder is *R*. Point target is located to constant φ surface at point, *P(x', 0, z')*.

The distance between a point in circumferential array element (x , z) and point *P(x' , z')* is,

$$r=\sqrt{(x-x')^2+(z-z')^2}$$

$$r=z'\sqrt{\frac{x^2}{z'^2}+\frac{x'^2}{z'^2}-\frac{2xx'}{z'^2}+1+\frac{z^2}{z'^2}-\frac{2z}{z'}}$$

$$z'>>x,\ \ z'>>z\Rightarrow r\approx z'\sqrt{\frac{x'^2}{z'^2}-\frac{2xx'}{z'^2}+1}$$

$$r\approx z'+\frac{x'^2}{2z'}-\frac{xx'}{z'}$$

Far field assumption is used. Ignore quadratic phase terms, and use $\sin\theta'=x'/z'$

➔ $r=-x\sin\theta'\Rightarrow$

$$PSF(\theta')=\int_{-\infty}^{\infty}A(x)e^{jkr}\,dx$$

Here $A(x)=circ(R)=\sqrt{R^2-x^2}$;

$$PSF(\theta')=\int_{-R}^{R}\sqrt{R^2-x^2}e^{jkx\sin\theta'}\,dx, x=R\sin\theta\Rightarrow dx=R\cos\theta d\theta$$ (variable transformation),

$$PSF(\theta')=\int_{-\pi/2}^{\pi/2}R^2\cos^2\theta e^{jkR\sin\theta'\sin\theta}\,d\theta$$

Using partial integration, $u=\cos\theta, dv=\cos\theta e^{jkR\sin\theta'\sin\theta}d\theta$;

Then Bessel identity; $J_n(u)=\frac{j^{-n}}{\pi}\int_{-\pi/2}^{\pi/2}\cos(n\phi)e^{ju\cos\phi}\,d\phi$ yields Equation 4.2,

$$PSF(\theta')=\pi R^2\frac{J_1(kR\sin\theta')}{kR\sin\theta'}$$

Curriculum Vitae

Publications:

[1] Sisman, A., Karaman, M., Gurun, G., Degertekin, F. L., "Solid-state SL IVUS Arrays Based on Non-uniform Aperture Sampling", *IEEE International Ultrasonics Symposium*, San Francisco (2010).

[2] Sisman, A., Karaman, M., Gurun, G., Degertekin, F. L., "Solid-state Arrays for Side-looking Intravascular Ultrasound Imaging", *IEEE Transactions on Ultrasonics Ferroelectronics and Frequency Control*. (To be submitted)

[3] Zahorian, J., Gurun, G., Guldiken, R., Balantekin, M., Degertekin, F.L., Karaman, M., Sisman, A., Qureshi, S., Hasler, P., Carlier, S. "Annular CMUT Arrays for Side-Looking Intravascular Imaging", *IEEE Transactions on Ultrasonics Ferroelectronics and Frequency Control*, (To be submitted)

[4] Sisman, A., Zahorian, J., Gurun, G., Karaman, M., Balantekin, M., Degertekin, F. L., Hasler, P. "Evaluation of CMUT Annular Arrays for Side-looking IVUS", *IEEE International Ultrasonics Symposium*, pp. 2774-2777 (2009)
Selected as one of the finalists in the Student Paper Competition

[5] Gurun, G., Sisman, A., Karaman, M., Hasler, P., Degertekin, F. L. "A Tunable Analog Delay Element for High-Frequency Dynamic Beamforming", *IEEE International Ultrasonics Symposium*, pp. 345-348 (2009)

[6] Sisman, A., Karaman, M., "Analysis of Catheter-based Imaging Devices for Side-looking IVUS," *BİYOMUT, 14th National Biomedical Engineering Meeting*, 1-4 (2009)

[7] Zahorian, J., Guldiken, R., Gurun, G., Qureshi, S., Balantekin, M., Carlier, S., Sisman, A., Karaman, M., Degertekin, F. L. "Annular CMUT Arrays for Side Looking Intravascular Ultrasound Imaging", *IEEE International Ultrasonics Symposium*, pp. 723-727 (2007)

[8] Sisman, A., Karaman, M., "Array Processing for 3D Ultrasound Imaging", *BİYOMUT, 12th National Biomedical Engineering Meeting*, (2007).

[9] Guldiken, R., Zahorian, J., Balantekin, M., Degertekin, F. L., Tekes, C., Sisman, A., Karaman, M., "Dual-Annular-Ring CMUT array for forward-looking IVUS imaging", *IEEE International Ultrasonics Symposium*, pp. 698-701 (2006).